

Broadband Ground-Motion Simulation Using a Hybrid Approach

by Robert W. Graves* and Arben Pitarka

Abstract This paper describes refinements to the hybrid broadband ground-motion simulation methodology of Graves and Pitarka (2004), which combines a deterministic approach at low frequencies ($f < 1$ Hz) with a semistochastic approach at high frequencies ($f > 1$ Hz). In our approach, fault rupture is represented kinematically and incorporates spatial heterogeneity in slip, rupture speed, and rise time. The prescribed slip distribution is constrained to follow an inverse wavenumber-squared fall-off and the average rupture speed is set at 80% of the local shear-wave velocity, which is then adjusted such that the rupture propagates faster in regions of high slip and slower in regions of low slip. We use a Kostrov-like slip-rate function having a rise time proportional to the square root of slip, with the average rise time across the entire fault constrained empirically. Recent observations from large surface rupturing earthquakes indicate a reduction of rupture propagation speed and lengthening of rise time in the near surface, which we model by applying a 70% reduction of the rupture speed and increasing the rise time by a factor of 2 in a zone extending from the surface to a depth of 5 km. We demonstrate the fidelity of the technique by modeling the strong-motion recordings from the Imperial Valley, Loma Prieta, Landers, and Northridge earthquakes.

Online Material: Station list, simulated and observed broadband waveforms, residual plots for acceleration response spectra, simulated and observed ShakeMaps, kinematic rupture model, and broadband wave-field animation.

Introduction

Our primary motivation in developing an enhanced broadband simulation methodology is to provide more robust estimates of the ground shaking expected in future earthquakes. Traditionally, ground-motion recordings from past earthquakes have been used as surrogates to represent the motions expected during future earthquakes. Unfortunately, the library of existing recordings only samples a small subset of possible earthquake scenarios. Thus, the ground-motion records typically must be scaled or modified in order to fit the magnitude, mechanism, distance, and site characteristics of the target earthquake. As an alternative, advances in the understanding of fault rupture processes, wave propagation phenomena, and site response characterization, coupled with the tremendous growth in computational power and efficiency, have made the prospect of large-scale ground-motion time series synthesis for future earthquakes much more feasible.

The process of numerically simulating broadband strong ground-motion time series is not new, and dates back at least to the groundbreaking work of Hartzell (1978) and Irikura (1978). These early studies proposed a method of summing

recordings of small earthquakes (empirical Green's functions) to estimate the response of a larger earthquake. Since then, the simulation techniques have been extended to include stochastic representation of source and path effects (e.g., Boore, 1983), theoretical full waveform Green's functions (e.g., Zeng *et al.*, 1994), or various combinations of these approaches (e.g., Hartzell *et al.*, 1999). Over the years, a large number of investigators have made significant contributions and refinements to these methodologies, most of which are based on kinematic descriptions of the rupture process. Hartzell *et al.* (1999) provides a comprehensive review and comparison of many of these existing kinematic simulation approaches. More recent studies have utilized fully spontaneous (Hartzell *et al.*, 2005) or dynamically constrained rupture characterizations (Pulido and Dalguer, 2009) to generate broadband ground-motion simulations. The dynamic approach is attractive because it alleviates the need for explicit prescription of kinematic rupture behavior, which in many cases must be based on simplifying assumptions and approximations. Unfortunately, our current level of knowledge regarding earthquake rupture dynamics is poorly constrained and suffers from a paucity of direct observational measurements, especially for those processes that affect higher frequency ground-motion radiation.

*Now at U.S. Geological Survey, 525 S. Wilson Avenue, Pasadena, California 91106, rwgraves@usgs.gov.

In our approach, the broadband ground-motion simulation procedure is a hybrid technique that computes the low-frequency and high-frequency ranges separately and then combines the two to produce a single time history (e.g., [Hartzell et al., 1999](#)). At frequencies below 1 Hz, the methodology is deterministic and contains a theoretically rigorous representation of fault rupture and wave propagation effects, and attempts to reproduce recorded ground-motion waveforms and amplitudes. At frequencies above 1 Hz, it uses a stochastic representation of source radiation, which is combined with a simplified theoretical representation of wave propagation and scattering effects. The use of different simulation approaches for the different frequency bands results from the seismological observation that source radiation and wave propagation effects tend to become stochastic at frequencies of about 1 Hz and higher, primarily reflecting our relative lack of knowledge about the details of these phenomena at higher frequencies. Recent variations of the hybrid approach include the work of [Liu et al. \(2006\)](#) and [Frankel \(2009\)](#).

A comprehensive and detailed description of the spatial and temporal characteristics of the rupture process is a necessary element of the broadband simulation procedure. [Liu et al. \(2006\)](#) propose the development of kinematic ruptures based on the correlation of random distributions of parameters such as slip, rupture velocity, and rise time. This work is continuing to develop through the use of dynamic rupture simulations (e.g., [Schmedes et al., 2010](#)) and the consideration of nonzero offsets in the coherency analysis (e.g., [Song et al., 2009](#)). In our approach, we have extended the slip and rupture speed correlation of [Graves and Pitarka \(2004\)](#) to include a magnitude dependent scaling; we have also adopted the slip and rise time correlation proposed by [Aagaard et al. \(2008\)](#).

Other recent improvements to our methodology are guided by studies that examine the depth-dependency of key rupture properties (e.g., [Mikumo, 1992](#); [Scholz, 2002](#)). Observations from recent earthquakes show that shallow rupturing events generate relatively weak high-frequency ground motions compared with deeper ruptures ([Kagawa et al., 2004](#); [Shearer et al., 2006](#); [Pitarka et al., 2009](#)). This type of behavior can be explained by velocity strengthening friction during fault rupture at shallow depths. Dynamically, it can be reproduced by including regions of negative stress drop during surface rupturing events ([Dalguer et al., 2008](#)), particularly when these regions are concentrated in the upper few kilometers of the rupture ([Marone and Scholz, 1988](#); [Pitarka et al., 2009](#)). During the rupture process, this leads to a reduction of rupture propagation speed and a lengthening of the rise time in these relatively weak zones of the fault. For large earthquakes, it has also been suggested that a similar transition region exists along the bottom edge of the fault, where the rupture progresses from an unstable to stable sliding mode as it crosses the brittle to ductile transition in the lower crust (e.g., [Hillers and Wesnousky, 2008](#); [Aagaard, Graves, Ma et al., 2010](#)).

Our methodology offers another significant enhancement over previous broadband simulation techniques through the use of frequency-dependent nonlinear site amplification factors based on a simple V_{S30} classification. [Graves and Pitarka \(2004\)](#) originally based these factors on the empirical relations of [Borcherdt \(1994\)](#); however, we have now extended this to incorporate the functions developed using equivalent linear response analysis as implemented in the empirical model of [Campbell and Bozorgnia \(2008\)](#). The use of V_{S30} is attractive because this parameter is readily available for most regions and the amplification functions are easy to compute and apply to large-scale simulations. The main drawbacks to the V_{S30} approach are the potential omission of detailed site-specific information about the soil column and the lack of phase modification in the resulting waveform.

In order to test the adequacy of our simulation methodology, we compare our computed synthetic strong-motion time histories with those recorded during past earthquakes. The only earthquake specific parameters we use are seismic moment, overall fault dimensions and geometry, hypocenter location, and a generalized model of the final slip distribution. For future earthquakes, these are the parameters that we feel can either be reliably estimated (e.g., seismic moment, fault dimensions) or parametrically assessed using multiple realizations (e.g., hypocenter location, slip distribution). All other source parameters are determined using the scaling relations described in the following sections. Since we have not optimized the rupture models for these exercises, we cannot hope to match all the details of the recorded waveforms. However, our goal is to reproduce the overall characteristics of the observed motions over a broad frequency range throughout the region surrounding the fault. This includes matching the trends and levels of common ground-motion parameters such as peak ground acceleration (PGA), peak ground velocity (PGV), response spectral acceleration (SA), and duration of shaking, adequately capturing near-fault phenomena such as rupture directivity and footwall/hanging wall effects, and reproducing region or site-specific effects such as basin response and site amplification.

Simulation Methodology

Source Characterization

The generation of a full kinematic rupture prescription requires specification of the spatially variable dislocation time function across the entire rupture surface. The necessary input parameters for this process are fault location and geometry (length, width, strike, and dip), seismic moment or magnitude, rupture initiation point (hypocenter), and slip direction (rake). In our formulation, the slip distribution is assumed to be random with a roughly wavenumber-squared spectral decay (e.g., [Herrero and Bernard, 1994](#); [Somerville et al., 1999](#); [Mai and Beroza, 2002](#)).

The rupture generation process begins with a uniform slip distribution having mild tapers at the sides and bottom of the

rupture surface (Fig. 1a). This is transformed to the wavenumber domain; using the procedure given in the Appendix, the spectrum is modified such that the wavenumber fall-off fits the von Karman correlation function given by Mai and Beroza (2002):

$$A(k_s, k_d) = \left[\frac{a_s a_d}{(1 + K^2)^{H+1}} \right]^{1/2}, \quad (1)$$

where

$$K^2 = a_s^2 k_s^2 + a_d^2 k_d^2 \quad (2)$$

is the normalized wavenumber ($k = 1/\text{wavelength}$), H is the Hurst exponent, and a_s and a_d are the along strike and down-dip correlation lengths, respectively. Following Mai and Beroza (2002), we set $H = 0.75$ and specify the magnitude dependent correlation lengths using the relations

$$\begin{aligned} \log_{10} a_s &= 0.5 \times M_w - 1.7 \\ \log_{10} a_d &= 0.333 \times M_w - 0.7. \end{aligned} \quad (3)$$

The resulting two-dimensional (2D) function is then transformed back to the spatial domain and scaled such that the target moment is achieved and the standard deviation of

the slip is 85% of the mean slip. One realization of this process is shown in Figure 1b. The spatial discretization (i.e., subfault size) of the final rupture model is on the order of 100 m.

In order to model ground motions for previous earthquakes, some information about the gross features of the slip distribution is necessary. In this situation, we begin with a low-pass filtered version of a slip model derived for the particular earthquake. Figure 1c shows an example of this for the Wald *et al.* (1991) slip model of the 1989 Loma Prieta earthquake. The filtering is done such that we retain only those wavelengths longer than the original subfault size used in the inversion. Then we add the higher wavenumbers using the method described previously. The resulting slip distribution for one realization of this process is shown in Figure 1d. Notice that while the long wavelength features of the original asperity distribution are generally preserved, the shorter length scales appear very similar in character to the purely random realization shown in Figure 1b.

Given an assumed hypocenter, rupture initiation times are then calculated using a two-step procedure. First, a background rupture speed distribution is given by

$$V_r = \begin{cases} 0.56 \times V_S & z < 5 \text{ km} \\ 0.8 \times V_S & z > 8 \text{ km} \end{cases}, \quad (4)$$

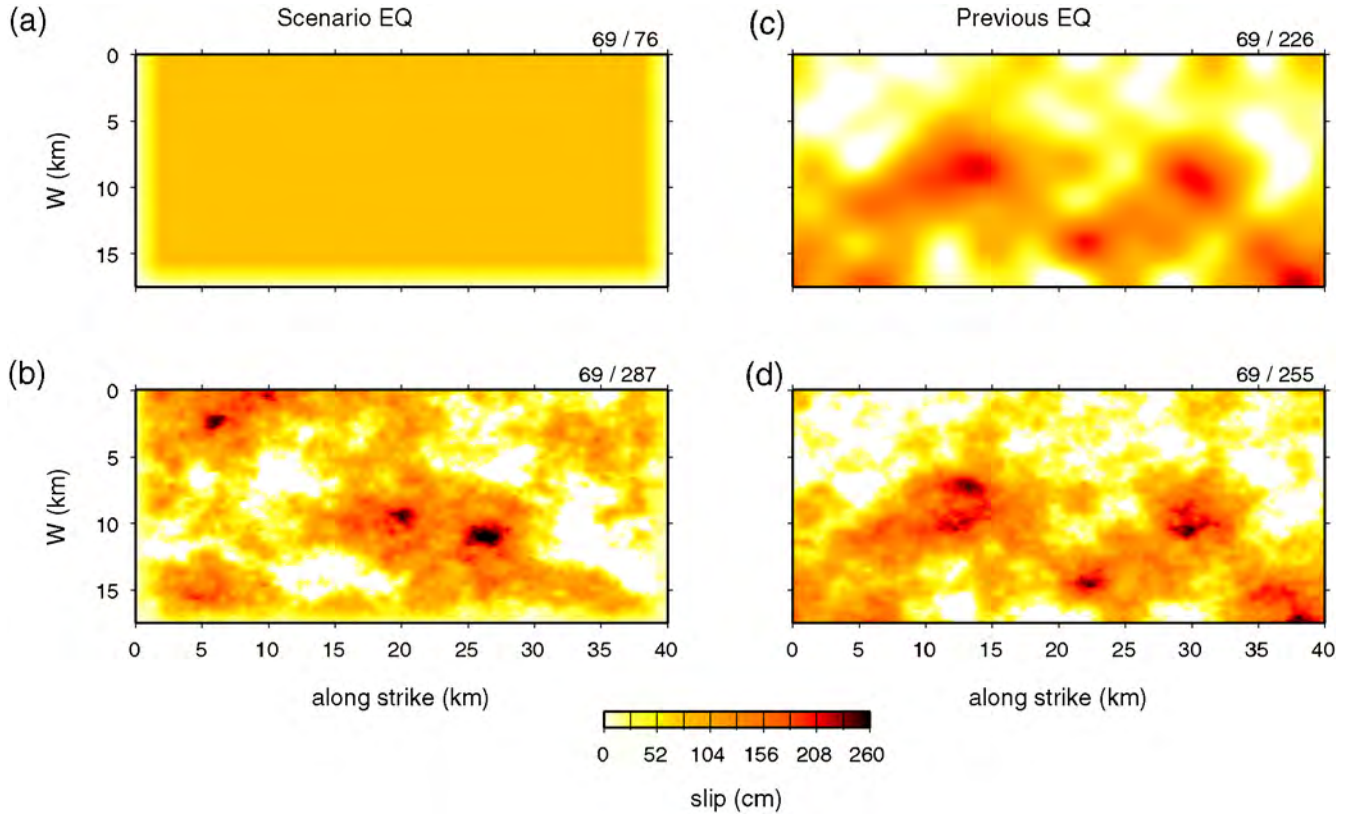


Figure 1. Examples of slip distributions generated using the wavenumber filtering approach with random phasing. (a), (b) For hypothetical scenario earthquakes, we start with uniform slip having (a) tapered edges and then apply wavenumber filtering and scaling such that (b) the standard deviation of the resulting slip distribution slip is 85% of the mean. (c), (d) For previous earthquakes, we start with (c) a low-pass filtered representation of the slip distribution, and then apply the same processing as with the scenario case to obtain (d) the final result. Mean and maximum slip values are indicated at top right of each panel. The color version of this figure is available only in the electronic edition.

where V_S is the local shear-wave velocity, z is depth, and a linear transition is applied between depths of 5 and 8 km. The value of 80% of V_S on the deeper portion of the fault is based on the average rupture speed determined for moderate and large crustal earthquakes by [Somerville *et al.* \(1999\)](#). The reduction of rupture speed by an additional 70% above 5 km is designed to represent the shallow weak zone in surface rupturing events (e.g., [Marone and Scholz, 1988](#); [Dauger *et al.*, 2008](#); [Pitarka *et al.*, 2009](#)) and is consistent with the results of [Shearer *et al.* \(2006\)](#) based on their analysis of numerous California earthquakes. The specific value of the reduction factor in this shallow zone is not that well constrained; however, we tried a range of values from 50% to 80% and found the value of 70% to produce the most favorable results. The choice of 5 km for the depth of the weak zone is based on the analysis of [Kagawa *et al.* \(2004\)](#). This background distribution is used to determine an initial estimate of the rupture front arrival time at the i th subfault, T_{i0} . The final value is then obtained by applying a timing perturbation that scales with the local slip:

$$T_{iF} = T_{i0} - \Delta t \left[\frac{\log(s_i) - \log(s_A)}{\log(s_M) - \log(s_A)} \right]. \quad (5)$$

Here s_i is the local slip value of the i th subfault (constrained here to have a minimum threshold of $0.05 s_A$), s_A is the average slip for the entire fault, s_M is the maximum slip on the fault, and the factor Δt scales with seismic moment as

$$\Delta t = 1.8 \times 10^{-9} \times M_o^{1/3}. \quad (6)$$

This scaling results in faster rupture propagation where the slip is large and slower rupture propagation where the slip is low, consistent with some models of dynamic rupture behavior (e.g., [Day, 1982](#)). The coefficient in equation (6) was determined by trial-and-error modeling with the general constraint that the maximum timing perturbations should be on the order of 1 to 2 s following the work of [Hisada \(2001\)](#). Additionally, we have assumed the timing perturbations scale with seismic moment in a self-similar manner. The top panel of [Figure 2](#) shows contours of rupture initiation times determined using this procedure for the Loma Prieta earthquake model and a hypocenter located in the middle of the fault near the bottom edge. The scaling given by equation (5) allows the rupture to snake across the larger slip patches of the fault as it propagates away from the hypocenter.

[Graves and Pitarka \(2004\)](#) proposed a slip-rate function constructed of two triangles following the work of [Güatteri *et al.* \(2004\)](#). Subsequent studies have proposed alternative dynamically compatible slip-rate functions based on combinations of convolution operators ([Tinti *et al.*, 2005](#)) or trigonometric functions ([Liu *et al.*, 2006](#)). All of these functions require specification of the final slip amount and the total slip duration. The [Tinti *et al.* \(2005\)](#) function also requires specification of an additional parameter, which is the time at which the peak slip velocity occurs. [Figure 3](#) compares these

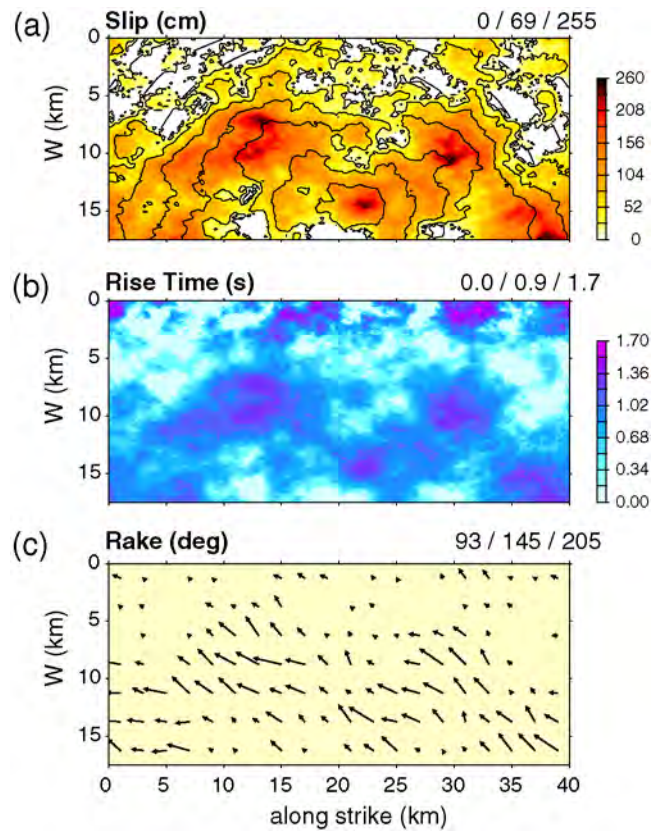


Figure 2. Kinematic rupture model developed for the Loma Prieta earthquake. (a) Panel shows slip distribution with rupture front contours at 1 s intervals super imposed, (b) panel shows distribution of slip rise time, and (c) panel shows distribution of rake. Triplet of numbers at top right of each panel indicates the minimum, mean and maximum values of the given distribution, respectively. The color version of this figure is available only in the electronic edition.

three functions and illustrates the close similarity among the formulations. For this comparison, we have set the time of the peak slip velocity in the [Tinti *et al.* \(2005\)](#) function to occur at 10% of the total slip duration. One advantage of the [Tinti *et al.* \(2005\)](#) and [Liu *et al.* \(2006\)](#) functions is that they eliminate the sharp corners in the triangle functions and have a smoother decay at the higher frequencies. Additionally, the [Liu *et al.* \(2006\)](#) function can be integrated analytically to derive a corresponding slip time function (e.g., [Aagaard, Graves, Ma *et al.*, 2010](#)). For these reasons, we have adopted the [Liu *et al.* \(2006\)](#) function in our current parameterization.

The duration of the slip-rate function is governed by the local rise time of the i th subfault, τ_i , which scales as

$$\tau_i = \begin{cases} 2 \times k \times s_i^{1/2} & z < 5 \text{ km} \\ k \times s_i^{1/2} & z > 8 \text{ km} \end{cases}, \quad (7)$$

with a linear transition between depths of 5 and 8 km. The depth scaling follows from [Kagawa *et al.* \(2004\)](#) who found a factor of 2 decrease in peak slip rate in the upper 5 km of surface rupturing events compared with deeper portions of the fault or to ruptures that do not break the surface.

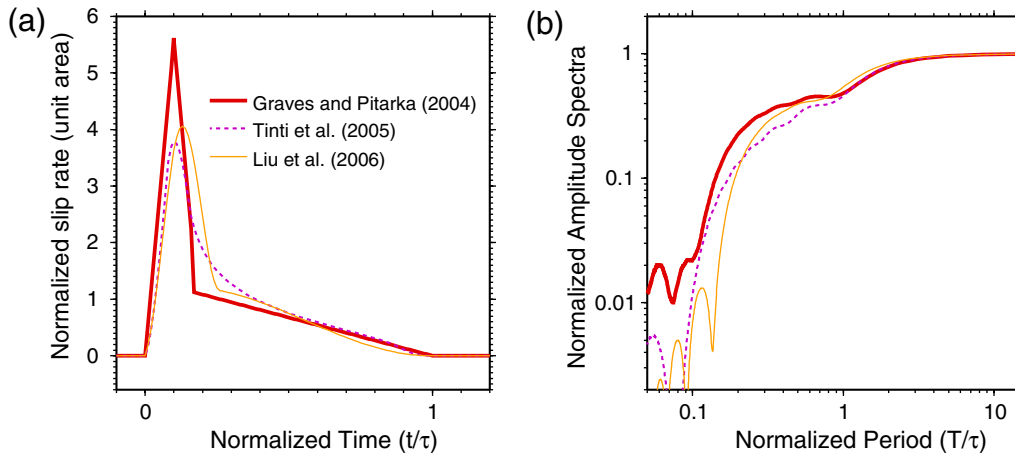


Figure 3. Comparison of kinematic slip-rate functions proposed by Graves and Pitarka (2004), Tinti *et al.* (2005), and Liu *et al.* (2006). (a) Panel shows functions in time domain and (b) panel shows Fourier amplitude spectra. The time of the peak velocity in the Tinti *et al.* (2005) function is set to occur at 10% of the total slip duration. All functions are normalized to have unit area. The slip rise time (τ) is defined to be the total nonzero extent of the function. The color version of this figure is available only in the electronic edition.

The choice of scaling with square root of local slip represents a trade-off between the end member cases of constant rise time and constant slip velocity (e.g., Aagaard *et al.*, 2008). The constant k in equation (7) is determined such that the average rise time over the entire fault is equal to the value given by a modified version of the Somerville *et al.* (1999) expression

$$\tau_A = \alpha_\tau \times 1.6 \times 10^{-9} \times M_o^{1/3}. \quad (8)$$

The factor α_τ scales the average rise time as a function of fault dip, δ ,

$$\alpha_\tau = \begin{cases} 1 & \delta > 60^\circ \\ 0.82 & \delta < 45^\circ \end{cases}, \quad (9)$$

where a linear transition is applied between dips of 60° and 45° . This scaling provides for a reduction of the rise time with decreasing fault dip to reflect the observed trend for reverse and thrust events (Somerville, 1998), with the shorter rise times for thrust events implying relatively high dynamic stress drops (Nielson and Olsen, 2000; Hartzell *et al.*, 2005). Although the factor α_τ is currently parameterized only as a function of fault dip, it should not be applied to normal faulting events because they occur under tension and presumably would have relatively low dynamic stress drops. Further calibration is needed to better constrain this factor for normal faulting events. Figure 2b plots the rise time distribution for the Loma Prieta earthquake model.

Finally, the slip direction (rake) is allowed to vary across the fault with a standard deviation of 15° about a prescribed mean value. The spatial distribution of the random rake variations follows a von Karman correlation function (Mai and Beroza, 2002) with the correlation lengths given by equation (3). The maximal rake variations are truncated at $\pm 60^\circ$. Figure 2c plots the rake distribution for the Loma Prieta earthquake model with a mean value of 135° .

Low-Frequency Simulation ($f < 1$ Hz)

The low-frequency portion of the simulation methodology uses a fully deterministic representation of source and wave propagation effects. The basic calculation is carried out using a parallelized three-dimensional (3D) visco-elastic, finite-difference algorithm (Graves, 1996) and incorporates both complex source rupture (as described previously) as well as wave propagation effects within arbitrarily heterogeneous 3D geologic structure. Anelastic attenuation is incorporated using the coarse-grain approach (Day and Bradley, 2001) with the quality factors given by the relations $Q_s = 50V_s$ (for V_s in km/s) and $Q_p = 2Q_s$. In the near surface layers, we set the minimum shear velocity at 0.5 km/s, which dictates a grid size of 0.1 km for the fourth order spatial finite-difference operators to achieve accurate results up to 1 Hz.

High-Frequency Simulation ($f > 1$ Hz)

The high-frequency portion of the simulation methodology has its roots in the pioneering work of Brune (1970) and Hanks and McGuire (1981), with the formal simulation approach for point sources first developed by Boore (1983) and the extension to finite-faults given by Frankel (1995), Beresnev and Atkinson (1997), and Hartzell *et al.* (1999). Recent work by Atkinson *et al.* (2009) and Boore (2009) provides systematic comparisons of the point-source and finite-fault stochastic formulations. In our approach, the fault is divided into a number of subfaults; we sum the response for each subfault assuming a random (stochastic) phase, a wave-number-squared source spectrum, and simplified Green's functions calculated for a specified one-dimensional (1D) velocity structure.

A basic premise of this approach is that it is designed to utilize the random phasing of the radiated subfault waveform to represent the poorly constrained and/or unknown details of

the rupture process. For this reason, we choose to limit the subfault size used for the high-frequency calculation to have a minimum characteristic dimension no smaller than about 1 km. Using smaller subfaults deteriorates the fidelity of the approach because as the number of subfaults used in the summation increases, the solution can become deficient for certain frequencies due to destructive interference of the random phasing (e.g., Joyner and Boore, 1986). The exact nature of these deficiencies and their frequency extent will depend on the specified rupture, the specified velocity structure, and the locations of the observation sites. While the specific choice of a minimum 1 km limit on subfault size is somewhat arbitrary, we have found this approach produces credible results, as will be demonstrated later by example.

In our approach, each subfault ($i = 1, N$) contributes an acceleration amplitude spectrum given by

$$A_i(f) = \sum_{j=1, M} C_{ij} S_i(f) G_{ij}(f) P(f), \quad (10)$$

where $\omega = 2\pi f$ is the angular frequency and the summation over $j = 1, M$ accounts for different rays (e.g., direct, Moho-reflected). The radiation scale factor C_{ij} is given by

$$C_{ij} = \frac{F_s R_{pij}}{4\pi \rho_i \beta_i^3}, \quad (11)$$

where $F_s = 2$ accounts for free surface amplification, R_{pij} is a conically averaged radiation pattern term spanning a range of $\pm 45^\circ$ in slip mechanism and take-off angle, and ρ_i and β_i are the density and shear-wave velocity at the center of the subfault. The source radiation spectrum is given by

$$S_i(f) = m_i F f^2 [1 + F(f/f_{ci})^2]^{-1}, \quad (12)$$

where $m_i = d_i \mu_i A_T / M_0$ is the relative seismic moment of the i th subfault and $F = M_0 / (N \sigma_p dl^3)$ is a factor introduced by Frankel (1995), which scales the subfault corner frequency to that of the mainshock and ensures the total moment of the summed subfaults is the same as the mainshock moment (M_0). The slip and rigidity of the i th subfault are given by d_i and μ_i , respectively; A_T is the total fault area; N is the total number of subfaults; σ_p is the Brune stress parameter (set 50 bars); and dl is the average subfault dimension. The subfault corner frequency is given by

$$f_{ci} = \frac{c_0 V_{Ri}}{\alpha_\tau \pi dl}, \quad (13)$$

where $c_0 = 2.1$ is an empirically determined constant, V_{Ri} is the local rupture speed at the subfault as given by equation (4), and α_τ is the dip related scale factor given by equation (9).

The path term is given by

$$G_{ij}(f) = \frac{I_i(f)}{r_{ij}} \exp \left[-\pi f^{1-x} \sum_{k=1, L} t_{ijk} / q_k \right], \quad (14)$$

where r_{ij} is the total path length of the j th ray from the i th subfault to the receiver and $I_i(f)$ represents gross impedance

effects calculated using quarter wavelength theory (Boore and Joyner, 1997) within the specified 1D velocity structure. Anelasticity is incorporated via a travel-time weighted average of the Q values for each of the velocity layers (Ou and Herrmann, 1990) with an assumed frequency dependence of the form $Q(f) = Q_o f^x$. The summation over $k = 1, L$ represents all of the ray path segments through the layers of the 1D velocity model, with t_{ijk} and q_k being the travel-time of the particular ray segment and Q value, respectively, within each velocity layer k . The constant Q of each velocity layer is modeled as a linear function of the shear-wave velocity

$$q_k = a + b \beta_k, \quad (15)$$

with the constants a and b determined empirically. Finally, the high-frequency spectral decay is modeled by Anderson and Hough (1984) as

$$P(f) = \exp(-\pi \kappa f). \quad (16)$$

Following the method of Boore (1983), the phase spectrum of the radiated acceleration for each ray is derived from a windowed time sequence of band-limited white Gaussian noise. We use a Saragoni and Hart (1974) windowing function with the peak of the envelope set at the direct S -wave arrival time with $\varepsilon = 0.2$ and $\eta = 0.05$ (see Boore, 1983, p. 1869). The duration of the window for the i th subfault is given by

$$T_{di} = f_{ci}^{-1} + c_1 R_i, \quad (17)$$

where $c_1 = 0.063$ is an empirically determined constant and R_i is the horizontal distance from the i th subfault to the receiver.

Site-Specific Amplification Factors

In the individual low-frequency and high-frequency calculations the minimum shear wave speed is set to 500 m/s and 865 m/s, respectively. This is done not only for computational efficiency, but also reflects our lack of sufficient knowledge regarding the detailed nature of the subsurface velocity structure, particularly in the upper few hundred meters. In order to account for site-specific geologic conditions in the final broadband response, we apply period-dependent, nonlinear amplification factors to the simulated time histories. These factors are based on the 30 m travel-time averaged shear-wave speed (V_{S30}) at the site of interest and were developed using equivalent linear site response analysis (Walling *et al.*, 2008) as implemented in the ground-motion prediction equation (GMPE) of Campbell and Bozorgnia (2008). We chose the formulation of Campbell and Bozorgnia (2008) because they employ separate terms for deep-basin amplification (which is explicitly included in our low-frequency calculation) and local site-specific amplification.

The site-specific amplification factors have the general form

$$F(T_i) = f(v_{\text{site}}, pga_R, T_i) / f(v_{\text{ref}}, pga_R, T_i), \quad (18)$$


where T_i are the discrete periods given by [Campbell and Bozorgnia \(2008\)](#); $f(x, y, z)$ is a function containing empirically derived, period-dependent coefficients; v_{site} denotes V_{S30} at the site of interest; v_{ref} corresponds to the V_{S30} used in the simulation; and pga_R denotes the rock level PGA from the short-period calculation. The amplification factors are applied to the low- and high-frequency responses separately because these have different reference site velocities. At each location in the simulation grid, we first obtain the site-specific $V_{S30}(v_{\text{site}})$ from the map of [Wills et al. \(2000\)](#); then v_{ref} is set to either the shear wave speed from the 3D velocity model for that location (low-frequency response) or the 1D velocity model (high-frequency response).

The amplification functions of [Campbell and Bozorgnia \(2008\)](#) are defined to a maximum spectral response period of 10 s. For periods greater than 1 s, we limit the level of the amplification factor to be no greater than its value at 1 s period and then taper to a level of unity from 5 to 10 s period. This is done to reduce the potential for overamplification of the longer periods, which are already included to a certain extent in the deterministic model, and to obtain a smooth transition for periods greater than 10 s.

We construct smoothly varying functions by linearly interpolating between the factors at the discrete periods and then apply these to the Fourier amplitude spectra of the simulated responses. Although the amplification factors are strictly defined for response spectra, the application in the Fourier domain is justified because the functions vary slowly with frequency. Once the amplification factors have been applied, we combine the individual low- and high-frequency responses into a single broadband time series using a set of matched fourth order Butterworth filters having a common corner frequency of 1 Hz ([Hartzell et al., 1999](#)).

Modeling of Past Earthquakes

1989 Loma Prieta Earthquake

Our model region for the Loma Prieta earthquake covers the area within about 100 km of the rupture surface, which includes 71 strong-motion recording sites. A detailed listing of these sites is given in the  electronic supplement to this paper. [Figure 4](#) shows a map view of the rupture surface and nearby recording sites. The site types range from BC to D ([Wills et al., 2000](#)). We have adopted a fault geometry and hypocenter following [Wald et al. \(1991\)](#) for our simulations. The fault is 40 km long and has a down-dip width of 17.5 km. The strike is 130° , dip is 70° , and the average rake is 135° . This model deviates slightly from the [Wald et al. \(1991\)](#) representation in that we have trimmed 2.5 km from the top edge of their fault since the slip is identically zero in this section. [Table 1](#) lists the fault parameters used for

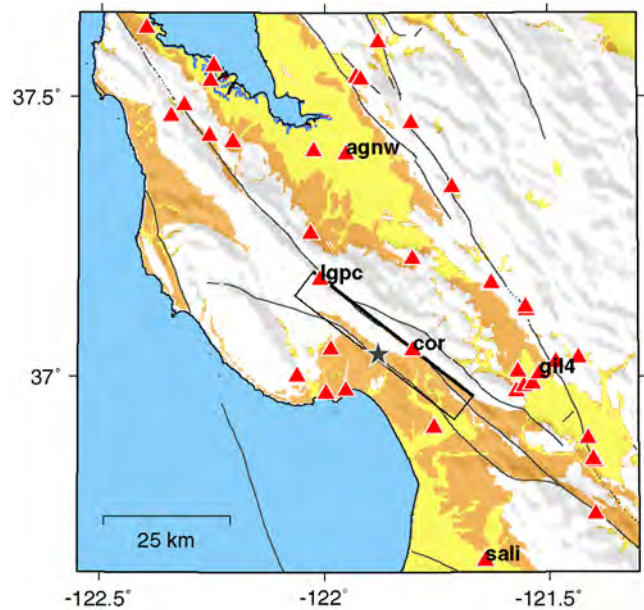


Figure 4. Map of the model region used for the Loma Prieta earthquake simulation. The rectangle indicates the surface projection of the fault with the heavy line denoting the top edge. The star is the epicenter and the triangles are recording stations analyzed in our study. Labeled stations are discussed in the text. Generalized surface geology follows the classification of [Wills et al. \(2000\)](#): white contains classes B, BC, and C; dark shading is CD; and light shading is class D. The color version of this figure is available only in the electronic edition.

our rupture model. We use a seismic moment of 1.83×10^{26} dyne-cm, giving a moment magnitude of 6.81. The rupture model used for this simulation has been discussed earlier and is shown in [Figure 2](#).

The subsurface velocity structure is based on version 08.3.0 of the U.S. Geological Survey 3D Bay Area Velocity Model (see the [Data and Resources](#) section). This model contains a 3D representation of the major geologic blocks and faults in the greater San Francisco Bay region, including the subsurface shape, depth, and properties of the major sedimentary basins, as well as the Conrad and Moho discontinuities and the structure of the upper mantle. For the low-frequency simulation, we discretize this model at a uniform grid spacing of 0.1 km and impose a minimum shear-wave velocity threshold of 0.5 km/s. For the high-frequency simulation, we construct a representative 1D velocity profile by averaging the profiles sampled at each of the strong-motion recording sites and also constraining V_{S30} to be 865 m/s. [Table 2](#) lists the Loma Prieta region 1D velocity model. High-frequency Q is modeled using equations (14) and (15), with $x = 0.6$, $a = 41$, and $b = 34$.

[Figure 5a,b](#) compares observed and simulated ground-velocity waveforms at five selected sites. Broadband motions are shown in [Figure 5a](#); low-pass filtered ($f < 0.5$ Hz) records are shown in [Figure 5b](#). These sites are indicated on the map shown in [Figure 4](#) and were chosen as a representative

Table 1
Fault Parameters for Validation Events

Earthquake	Longitude Top Center*	Latitude Top Center*	Depth [†] (km)	Length (km)	Width (km)	Strike (°)	Dip (°)
Loma Prieta	−121.841	37.079	3.85	40	17.5	128	70
Northridge	−118.515	34.344	5.00	20	25	122	40
Landers segment 1	−116.630	34.606	0	27	15	140	90
Landers segment 2	−116.497	34.440	0	21	15	154	90
Landers segment 3	−116.440	34.228	0	30	15	175	90
Imperial Valley	−115.412	32.739	0	39	10.5	143	90

*Longitude and latitude are given for the top center location of the fault plane.

[†]Depth is given from the surface to the top of the fault plane.

sample spanning the region covered by the simulation. Because we are using a generalized rupture model of this earthquake that incorporates only limited information about the actual rupture, we cannot hope to match all the details of the recorded waveforms. In general the amplitude, duration, and frequency content of the observed waveforms are matched reasonably well by the simulation for these sites. In the near-fault region (LGPC and COR), the motions are pulselike and relatively brief. Station LGPC experiences strong rupture directivity resulting in a concentrated pulse of motion on the fault-normal (218° azimuth) component of motion. At COR, which is close to the epicenter, the motions are richer in high frequencies and the amplitude is roughly the same on fault-normal and fault-parallel (128° azimuth) components. To the north in the Santa Clara basin (AGNW), the waves begin to interact with the 3D structure, generating a complex set of arrivals. The simulation generally matches this character, although it tends to produce stronger later-arriving surface waves than are seen in the data. The stations at GIL4 and SATI are also situated on small sedimentary basin structures that give rise to later-arriving lower frequency motions following the higher frequency direct

arrivals. Again, these characteristics are matched reasonably well by the simulation.

We have measured the peak ground acceleration (PGA) and peak ground velocity (PGV) for the observed and simulated motions at all 71 sites used in our model. Here the PGA and PGV are defined to be the geometric mean of these values measured from the north–south and east–west horizontal components of motion. Figure 6 plots the PGA and PGV as functions of distance from the rupture plane. The level and trend of the observed values are matched well by the simulation. The amount of variability (scatter) in the simulated PGA is somewhat lower than the observed values, while for PGV, the simulations exhibit a similar level of variability as seen in the observations. Also shown in Figure 6 are PGA and PGV residuals plotted as functions of distance and separated into sites having V_{S30} above and below 400 m/s. There is little systematic trend in these residuals for distances out to about 60 km. The sites beyond 60 km are primarily located in and around San Francisco, and the simulation generally underpredicts the PGA and PGV at these sites. We have also computed residuals for 5% damped spectral acceleration, which indicate the underprediction at these more distant sites is limited to periods less than about 1 s. Plots of these residuals are included in the $\text{\textcircled{E}}$ electronic supplement to this paper. Previous studies (e.g., Somerville and Yoshimura, 1990) have demonstrated the importance of critical Moho reflections to the ground-motion response at these sites. Aagaard, Brocher, Dolenc, Dreger, Graves, Harmsen, Hartzell, Larsen, and Zoback (2008) estimate that for sites in this distance range, the Moho reflections account for an increase in PGA level of about 35% and in PGV level of about 15%. Because our simulation includes the effect of Moho reflections for both the low- and high-frequency portions of the model, we suspect that this underprediction results from deficiencies in our assumed 3D velocity model and/or deficiencies in our assumed site response model.

We also compare the data and simulations using the model bias and standard error for 5% damped spectral acceleration calculated from the broadband time series (e.g., Schneider *et al.*, 1993). For the j th station, the residual between the observed and simulated spectral acceleration at a period T_i is given by

$$r_j(T_i) = \ln[O_j(T_i)/S_j(T_i)], \quad (19)$$

Table 2

Loma Prieta Region 1D Velocity Profile

Thickness (km)	V_p (km/s)	V_s (km/s)	Density (g/cm ³)
0.002	1.70	0.45	2.00
0.004	1.80	0.65	2.10
0.006	1.80	0.85	2.10
0.008	1.90	0.95	2.10
0.01	2.00	1.15	2.20
0.07	2.40	1.20	2.20
0.10	2.60	1.30	2.40
0.30	3.00	1.40	2.45
0.50	3.60	1.95	2.55
0.50	4.40	2.50	2.60
1.00	4.80	2.80	2.60
1.00	5.25	3.10	2.62
1.50	5.50	3.25	2.65
2.00	5.60	3.35	2.70
2.00	5.75	3.45	2.72
8.00	6.10	3.60	2.75
8.00	6.50	3.80	3.00
–	7.80	4.40	3.30

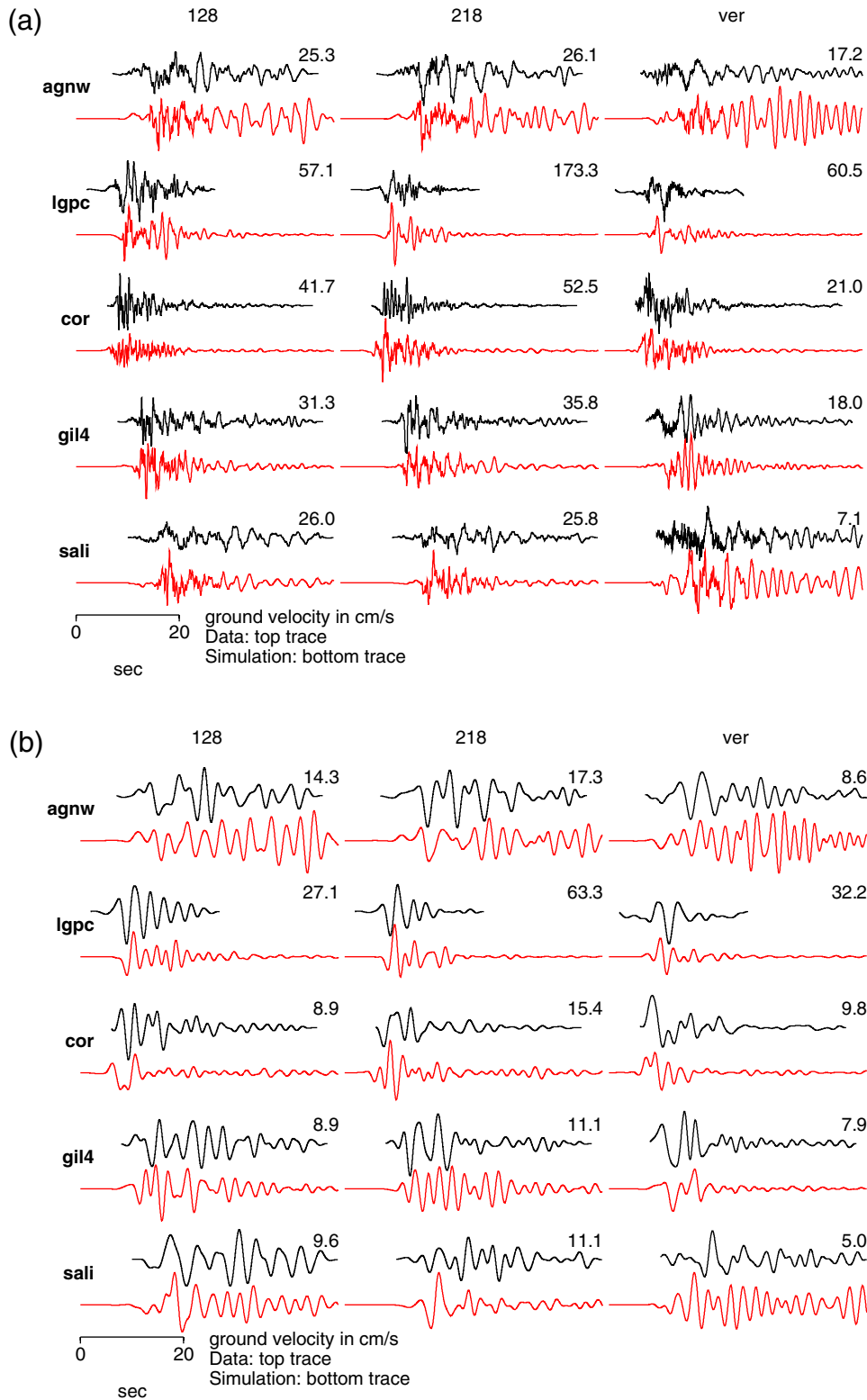


Figure 5. (a) Comparison of recorded (top) and simulated (bottom) broadband three-component ground-velocity waveforms at five selected sites for the Loma Prieta earthquake. Horizontal components have been rotated into fault-parallel (128° azimuth) and fault-normal (218° azimuth) orientations. Station locations are indicated in Figure 4. The recorded and simulated motions for each component and station are scaled to the maximum value listed above each pair of waveforms. (b) Comparison of recorded (top) and simulated (bottom) low-pass filtered ($f < 0.5$ Hz) three-component ground-velocity waveforms at five selected sites for the Loma Prieta earthquake. Horizontal components have been rotated into fault-parallel (128° azimuth) and fault-normal (218° azimuth) orientations. Station locations are indicated in Figure 4. The recorded and simulated motions for each component and station are scaled to the maximum value listed above each pair of waveforms. The color version of this figure is available only in the electronic edition.

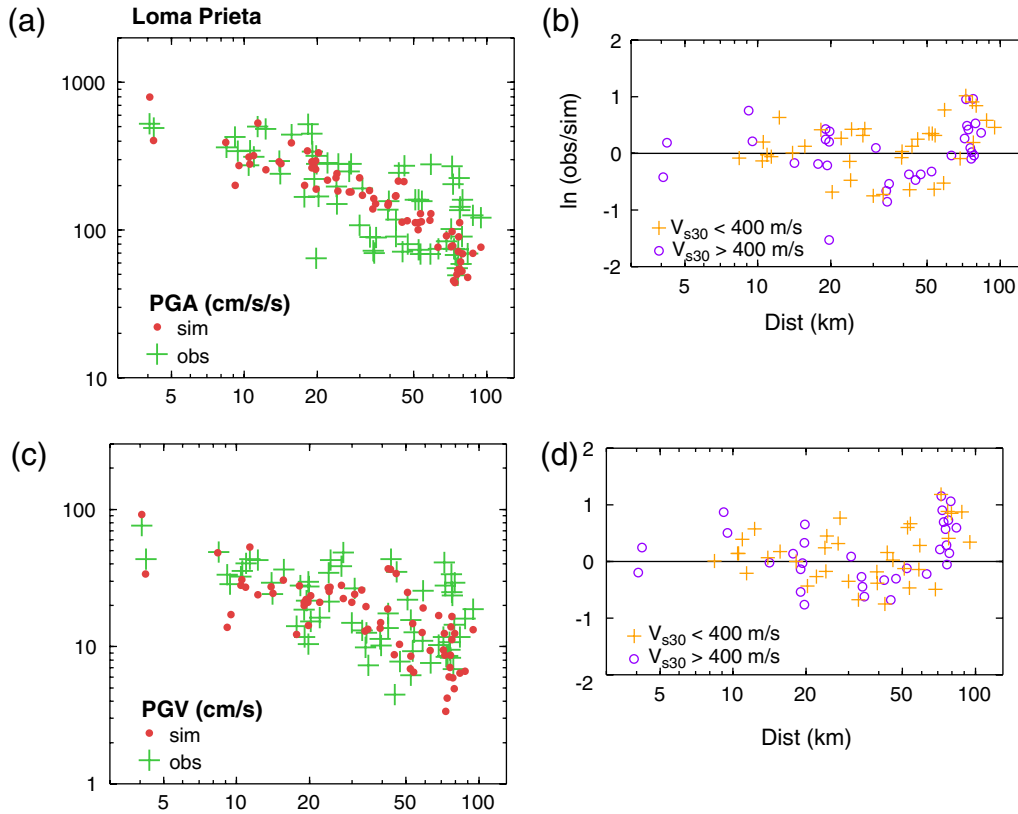


Figure 6. (a), (b) Comparison of recorded and simulated PGA and (c), (d) PGV plotted as functions of closest distance to the fault surface for the Loma Prieta earthquake. (a), (c) Panels show absolute ground-motion values (recorded as crosses, simulated as circles) and (b), (d) panels show the residuals of the recorded and simulated values in natural log units. For residuals, sites have been separated into two groups based on V_{s30} . The color version of this figure is available only in the electronic edition.

where $O_j(T_i)$ and $S_j(T_i)$ are the observed and simulated values on a given component, respectively. The model bias is then given by

$$B(T_i) = \frac{1}{N} \sum_{j=1, N} r_j(T_i), \quad (20)$$

and the standard error is given by

$$\sigma(T_i) = \left\{ \frac{1}{N} \sum_{j=1, N} [r_j(T_i) - B(T_i)]^2 \right\}^{1/2}, \quad (21)$$

where N is the total number of stations. Figure 7 shows the model bias and standard error for the Loma Prieta simulation. For this comparison, we compute separate measures for the horizontal components of motion oriented in the fault-parallel (128° azimuth) and fault-normal (218° azimuth) orientations, as well as their geometric mean (average horizontal); we only consider sites in the near-fault region, that is, those located within one fault length (40 km) of the rupture surface. There are a total of 36 sites within this distance range. The comparisons shown in Figure 7 exhibit little systematic model bias across a wide frequency range. This is true for the average horizontal component as well as for the individual fault-normal and fault-parallel components. The standard error ranges from about 0.4 to 0.6 natural log units.

1994 Northridge Earthquake

Our model region for the Northridge earthquake covers the area within about 70 km of the rupture surface, which includes 133 strong-motion recording sites. A detailed listing of these sites is given in the $\text{\textcircled{E}}$ electronic supplement to this paper. Figure 8 shows a map view of the rupture surface and nearby recording sites. The site types range from BC to D (Wills *et al.*, 2000). We have adopted a fault geometry and hypocenter following Hartzell *et al.* (1996) for our simulations. The fault is 20 km long and has a down-dip width of 25 km. The strike is 122° , dip is 40° , and the average rake is 101° . Table 1 lists the fault parameters used for our rupture model. We use a seismic moment of 1.17×10^{26} dyne-cm, giving a moment magnitude of 6.68. Our rupture model is derived starting from a low-pass version of the Hartzell *et al.* (1996) slip distribution, and then following the steps described earlier to develop the full kinematic description. Previous studies of the Northridge earthquake have found this event is characterized by a relatively brief slip rise time, resulting in an increased level of shorter period energy release indicative of a relatively high dynamic stress drop rupture (e.g., Wald *et al.*, 1996; Hartzell *et al.*, 1996; Beresnev and Atkinson, 1998; Hartzell *et al.*, 2005). We account for this observation using the dip-dependent scaling given by

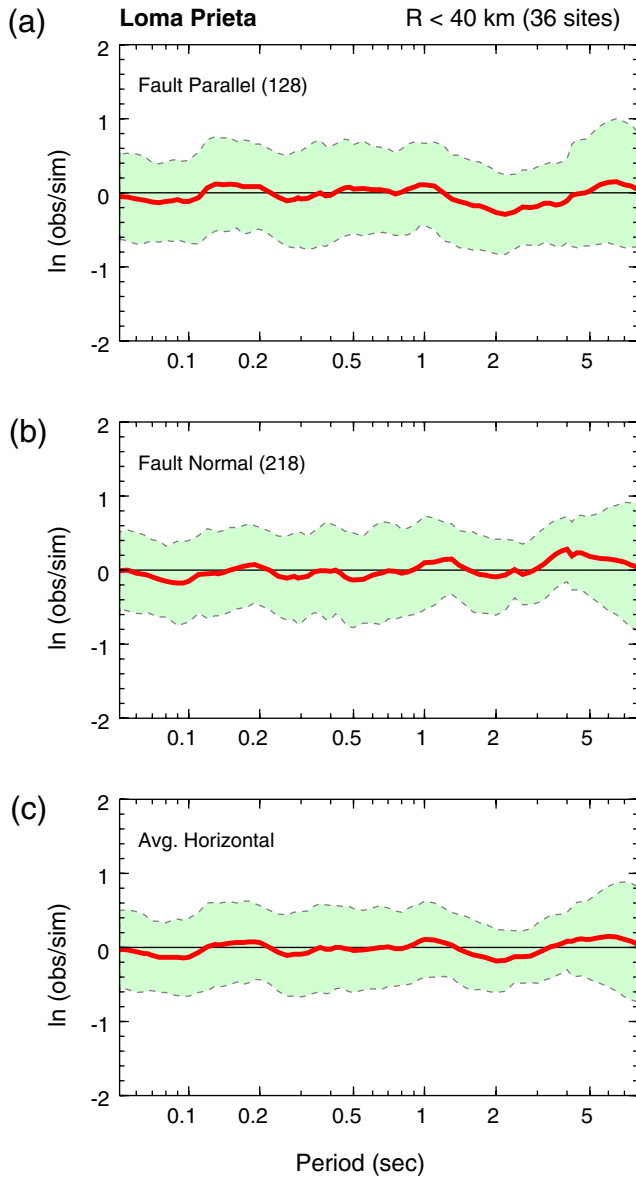


Figure 7. Model bias (heavy line) and standard error (shaded region) for 5% damped spectral acceleration using 36 sites for the Loma Prieta earthquake. (a) Panel is for fault-parallel component, (b) panel is for fault-normal component, and (c) panel is for the average horizontal (geometric mean) component. The color version of this figure is available only in the electronic edition.

equation (9), which results in an 18% decrease in rise time and a 22% increase in corner frequency. The rupture model used for our simulations is shown in Figure 9.

The subsurface velocity structure is based on version 4 of the Southern California Earthquake Center (SCEC) Community Velocity Model (CVM4; see the [Data and Resources](#) section). This model contains a 3D representation of the major geologic blocks and faults in the greater Los Angeles region, including the subsurface shape, depth, and properties of the major sedimentary basins as well as the Moho discontinuity and the structure of the upper mantle. In regions outside of the sedimentary basins, the SCEC

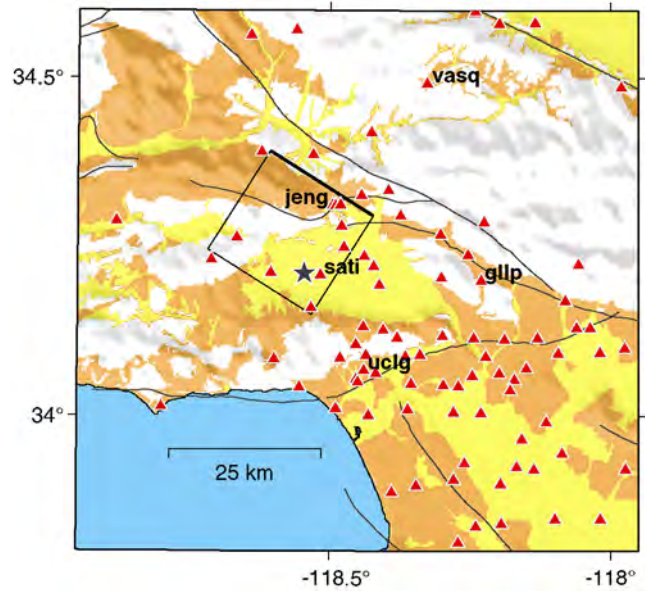


Figure 8. Map of the model region used for the Northridge earthquake simulation. The rectangle indicates the surface projection of the fault with the heavy line denoting the top edge. The star is the epicenter and the triangles are recording stations analyzed in our study. Labeled stations are discussed in the text. Generalized surface geology follows the classification of [Wills et al. \(2000\)](#): white contains classes B, BC, and C; dark shading is CD; and light shading is class D. The color version of this figure is available only in the electronic edition.

CVM4 has unrealistically high velocities in the near surface material, typically with shear-wave velocities of about 3 km/s. Using the generic rock site profile proposed by [Boore and Joyner \(1997\)](#), we have modified this model to include a velocity taper in the near surface for these nonbasin regions. This gives more reasonable shear-wave velocities of about 0.8 to 1 km/s in the near surface. For the low-frequency simulation, we discretize the model at a uniform grid spacing of 0.1 km and impose a minimum shear-wave velocity threshold of 0.5 km/s. For the high-frequency simulation, we construct a representative 1D velocity profile by averaging the profiles sampled at each of the strong-motion recording sites and also constraining V_{S30} to be 865 m/s. Table 3 lists the Northridge region 1D velocity model. High-frequency Q is modeled using equations (14) and (15), with $x = 0.6$, $a = 41$, and $b = 34$.

Figure 10a,b compares observed and simulated ground-velocity waveforms at five selected sites. Broadband motions are shown in Figure 10a, and low-pass filtered ($f < 0.5$ Hz) records are shown in Figure 10b. These sites are indicated on the map shown in Figure 8 and were chosen as a representative sample spanning the region covered by the simulation. Because we are using a generalized rupture model of this earthquake that incorporates only limited information about the actual rupture, we cannot hope to match all the details of the recorded waveforms. As with the Loma Prieta simulation, the amplitude, duration, and frequency content of the

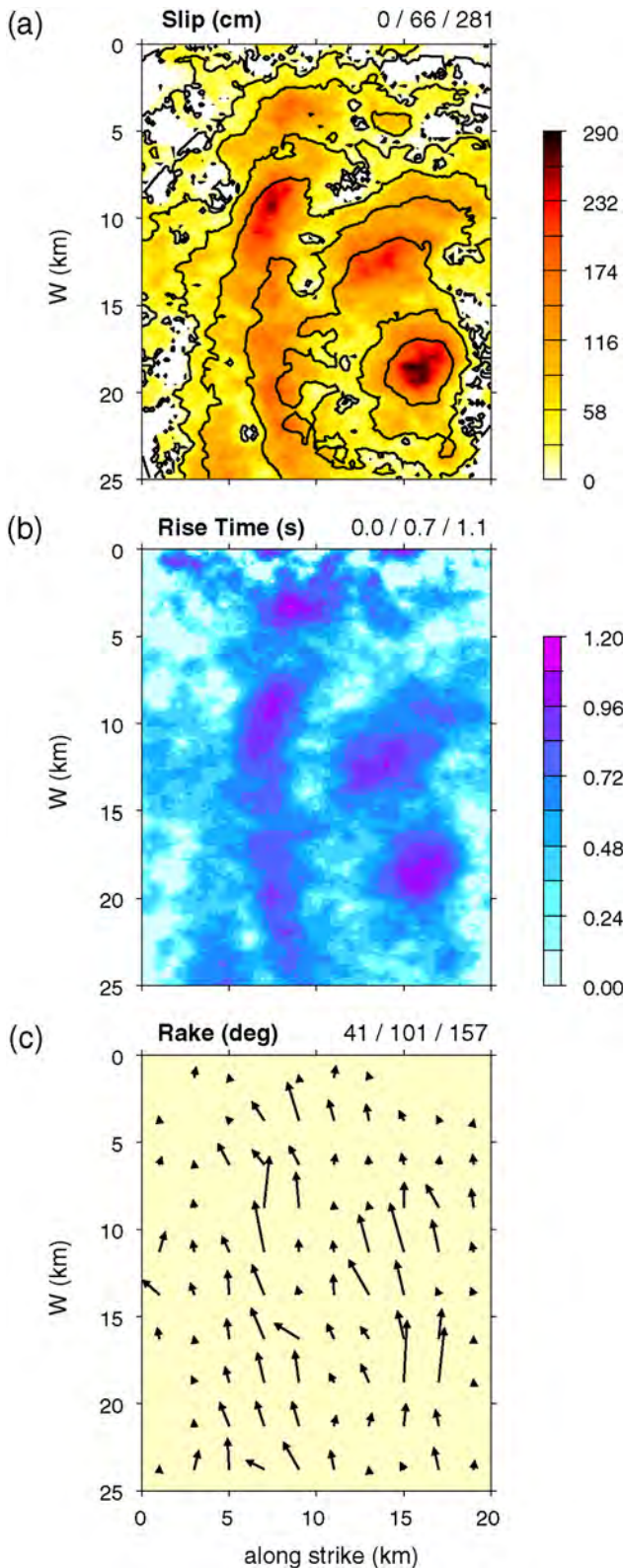


Figure 9. Kinematic rupture model developed for the Northridge earthquake. (a) Panel shows slip distribution with rupture front contours at 1 s intervals super imposed, (b) panel shows distribution of slip rise time, and (c) panel shows distribution of rake. Triplet of numbers at top right of each panel indicates the minimum, mean and maximum values of the given distribution, respectively. The color version of this figure is available only in the electronic edition.

observed waveforms are matched reasonably well by the simulation for these sites. The Northridge event produced strong rupture directivity effects toward the north. These effects are readily seen in the observed and simulated waveforms at station JENG where the motions are concentrated into brief pulslike arrivals, which are strongest on the fault-normal (212° azimuth) horizontal component. Relatively strong shaking also occurred near the epicenter at SATI, although the duration of strong shaking is longer compared with JENG; multiple later arrivals generated within the sediments of the San Fernando basin are apparent in the waveforms. Further to the south (UGLG), the waves enter the northern margin of the Los Angeles basin where the largest amplitude arrivals are basin-generated surface waves, which follow the first arriving S waves by several seconds. In comparison to these basin sites, the response at the stiffer sites of GLLP and VASQ are characterized by higher frequency and relatively shorter duration motions, which are also reproduced in the simulations.

We compare observed and simulated PGA and PGV as functions of closest distance to the rupture surface in Figure 11. Both the level and trend of the observations are matched quite well by the simulation. As was noted for the Loma Prieta simulation, the amount of variability produced by the simulation is less than that observed for PGA, but is closer to that observed for PGV. The residuals shown in Figure 11b,d show little systematic bias either as a function of distance or site type. Additionally, a similar result is found for 5% damped spectral acceleration at periods ranging from 0.05 to 5 s (see the [E](#) electronic supplement to this paper).

Using equations (19), (20), and (21), we compute the model bias and standard error for 5% damped spectral acceleration over a suite of periods from 0.05 to 8 s for the Northridge simulation. The results are displayed in Figure 12 for the fault-parallel (122° azimuth), fault-normal (212° azimuth),

Table 3
Northridge Region 1D Velocity Profile

Thickness (km)	V_p (km/s)	V_s (km/s)	Density (g/cm ³)
0.002	1.70	0.45	2.00
0.004	1.80	0.65	2.10
0.006	1.80	0.85	2.10
0.008	1.90	0.95	2.10
0.01	2.00	1.15	2.20
0.07	2.40	1.20	2.20
0.20	2.80	1.40	2.30
0.20	3.10	1.60	2.40
0.20	3.40	1.80	2.45
0.30	3.70	2.10	2.50
2.00	4.40	2.40	2.60
2.00	5.10	2.80	2.70
1.00	5.60	3.15	2.75
5.00	6.15	3.60	2.825
5.00	6.32	3.65	2.85
5.00	6.55	3.70	2.90
10.00	6.80	3.80	2.95
–	7.80	4.50	3.20

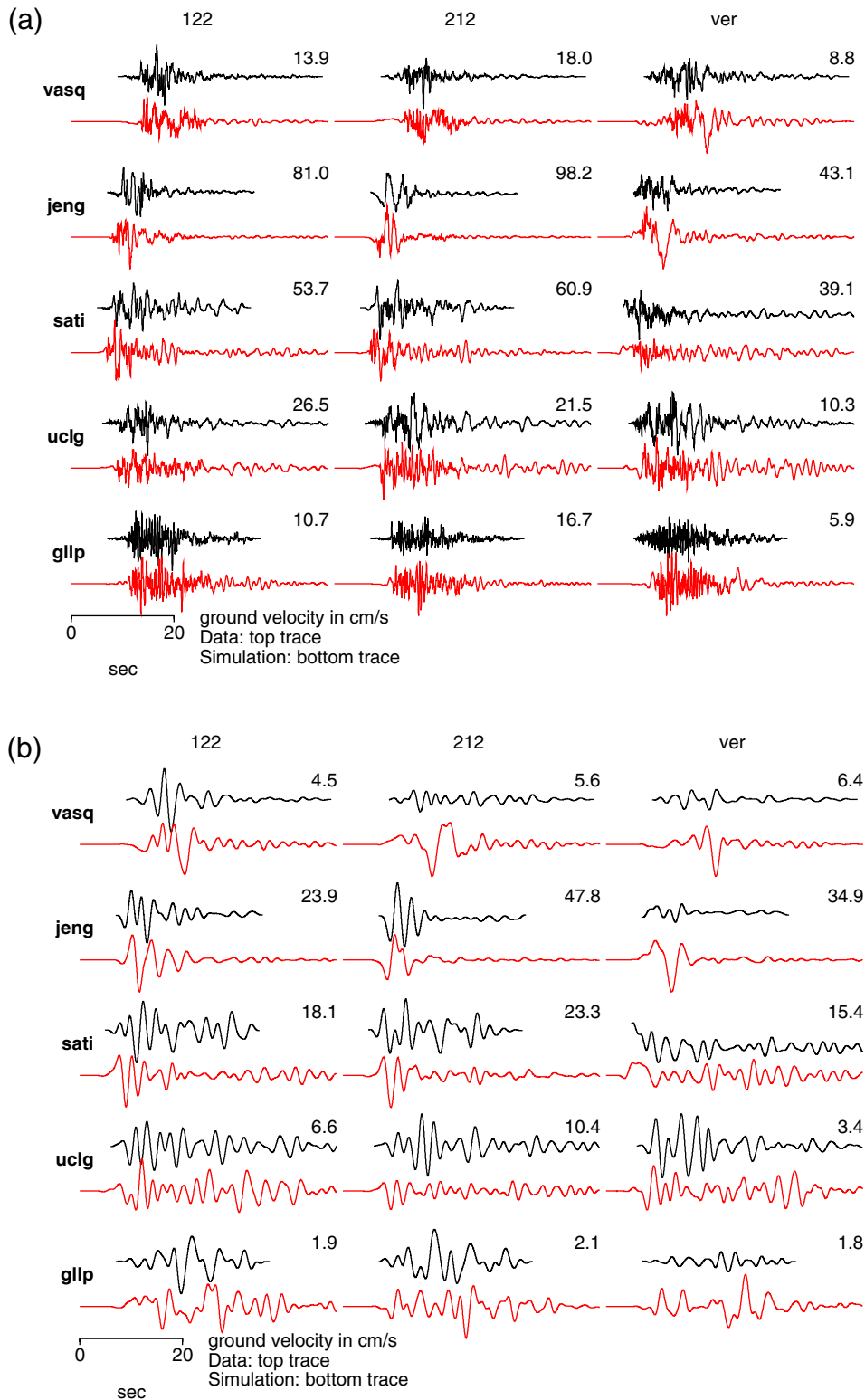


Figure 10. (a) Comparison of recorded (top) and simulated (bottom) broadband three-component ground-velocity waveforms at five selected sites for the Northridge earthquake. Horizontal components have been rotated into fault-parallel (122° azimuth) and fault-normal (212° azimuth) orientations. Station locations are indicated in Figure 8. The recorded and simulated motions for each component and station are scaled to the maximum value listed above each pair of waveforms. (b) Comparison of recorded (top) and simulated (bottom) low-pass filtered ($f < 0.5$ Hz) three-component ground-velocity waveforms at five selected sites for the Northridge earthquake. Horizontal components have been rotated into fault-parallel (122° azimuth) and fault-normal (212° azimuth) orientations. Station locations are indicated in Figure 8. The recorded and simulated motions for each component and station are scaled to the maximum value listed above each pair of waveforms. The color version of this figure is available only in the electronic edition.

and average horizontal (geometric mean) components. This comparison is limited to sites having a closest distance within 25 km from the rupture, yielding a total of sites. The model bias is near zero for all components across the entire bandwidth, indicating that, on average, the simulation is accurately reproducing the main characteristics of the observed ground motions. Additionally, the standard error for these comparisons is about 0.4 to 0.5 natural log units.

1992 Landers Earthquake

Our model region for the Landers earthquake covers the area within about 100 km of the rupture surface, which includes 23 strong-motion recording sites. A detailed listing of these sites is given in the $\text{\textcircled{E}}$ electronic supplement to this paper. Figure 13 shows a map view of the rupture planes and nearby recording sites. The site types range from BC to D (Wills *et al.*, 2000). We have adopted a fault geometry and hypocenter following Wald and Heaton (1994) for our simulations. The fault is composed of three segments, all having a dip of 90° and down-dip width of 15 km. We have collapsed the overlapping portions of the segments from the Wald and Heaton (1994) model so that the individual segments abut one another. From north to south, the segments have lengths of 27, 21, and 30 km and strike directions of

140° , 154° , and 175° , respectively. The average rake is 180° . Table 1 lists the fault parameters used for our rupture model. We use a total seismic moment of 6.16×10^{26} dyne-cm, giving a moment magnitude of 7.16.

Our rupture model is derived starting from a low-pass version of the Wald and Heaton (1994) strong-motion slip distribution with the modification that we increase the slip by 100 cm in a 9 km by 7.5 km patch surrounding the hypocenter. This was necessary in order to match the level of ground motions observed to the south of the rupture where we have about twice the number of observation sites as used in the Wald and Heaton (1994) source inversion study. The full kinematic description is then developed following the steps described earlier with one refinement. In order to model the effect of rupture propagating from one fault segment to another, we apply a 50% reduction of the rupture propagation speed within 4 km of each segment boundary. This delays the rupture as it jumps from segment to segment, consistent with source modeling studies (e.g., Wald and Heaton, 1994) and dynamic rupture simulations (e.g., Harris and Day, 1999). The rupture model developed for our simulations is shown in Figure 14. Although the pattern of rupture propagation is rather complex, the delay in rupture speed across the segment boundaries is evident from the rupture initiation contours

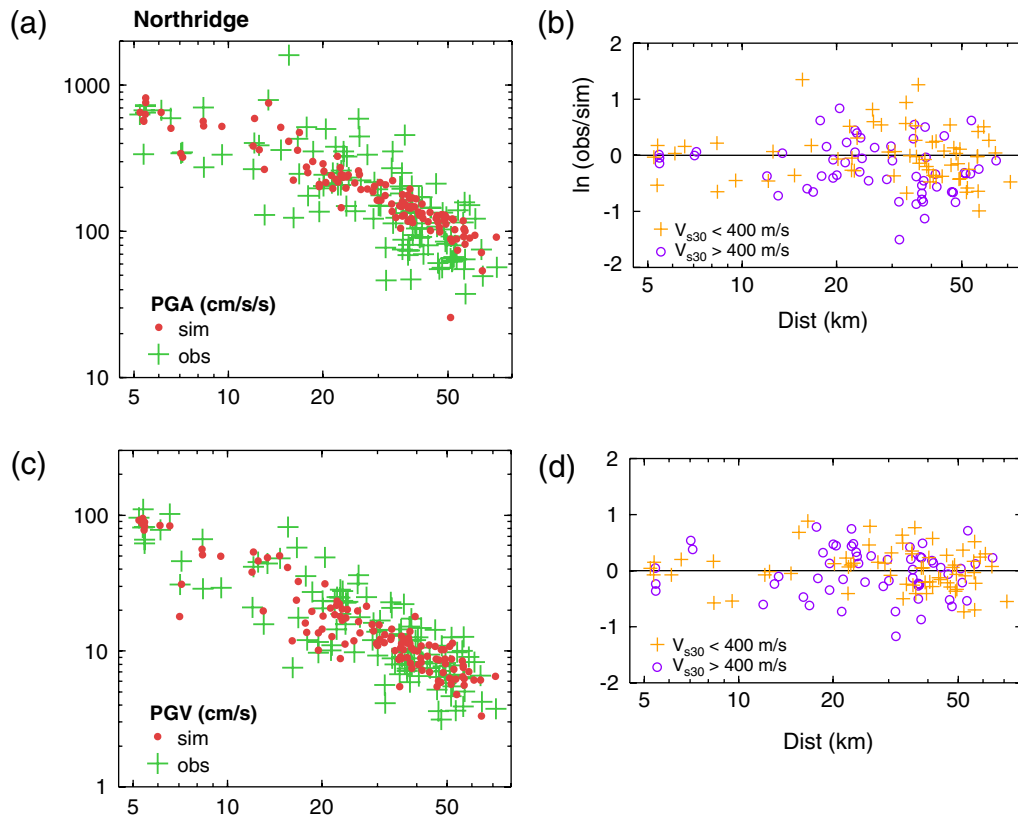


Figure 11. (a), (b) Comparison of recorded and simulated PGA and (c), (d) PGV plotted as functions of closest distance to the fault surface for the Northridge earthquake. (a), (c) Panels show absolute ground-motion values (recorded as crosses, simulated as circles) and (b), (d) panels show the residuals of the recorded and simulated values in natural log units. For residuals, sites have been separated into two groups based on V_{s30} . The color version of this figure is available only in the electronic edition.

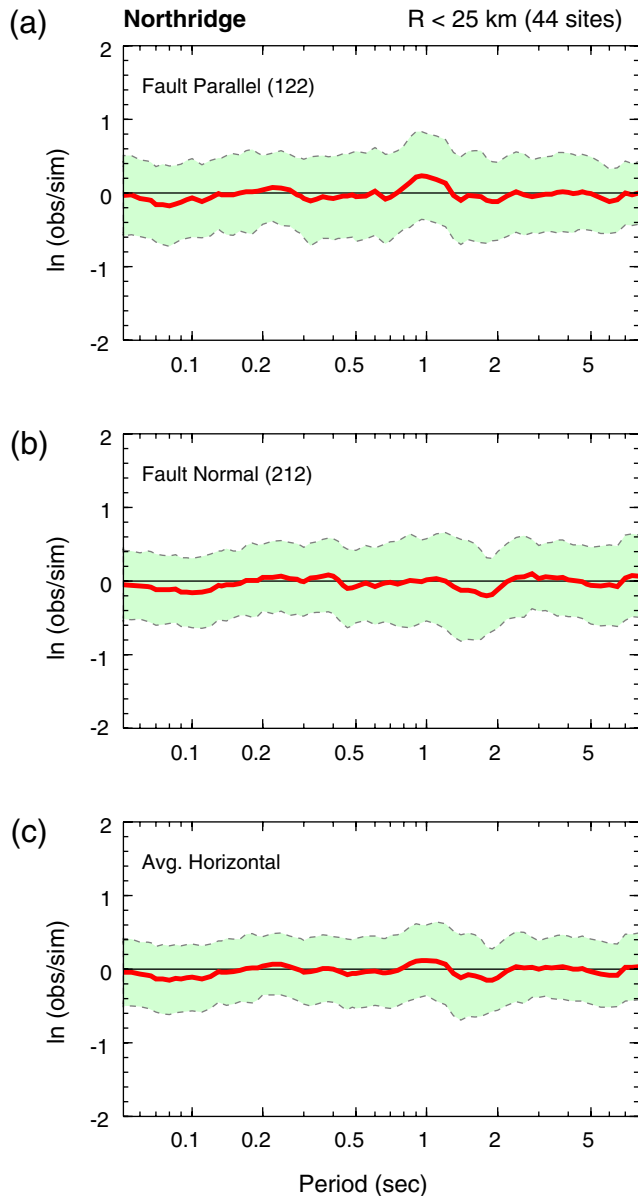


Figure 12. Model bias (heavy line) and standard error (shaded region) for 5% damped spectral acceleration using 44 sites for the Northridge earthquake. (a) Panel is for fault-parallel component, (b) panel is for fault-normal component, and (c) panel is for the average horizontal (geometric mean) component. The color version of this figure is available only in the electronic edition.

shown in the top panel of this figure. Additionally, the slowing of the rupture and the lengthening of the rise time within the upper 5 km (from equations 4 and 7) are also quite clear.

The subsurface velocity structure is based on the SCEC CVM4, modified to include the Boore and Joyner (1997) generic rock velocity structure in the near surface of the non-basin portions of the model. For the low-frequency simulation, we discretize this model at a uniform grid spacing of 0.1 km and impose a minimum shear-wave velocity threshold of 0.5 km/s. For the high-frequency simulation, we construct a representative 1D velocity profile by averaging the

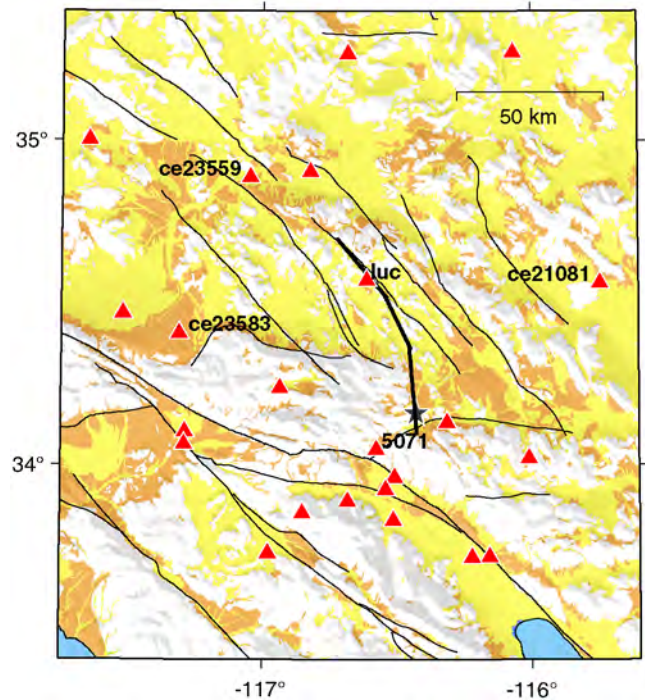


Figure 13. Map of the model region used for the Landers earthquake simulation. The heavy lines indicate the surface traces of the three fault segments. The star is the epicenter and the triangles are recording stations analyzed in our study. Labeled stations are discussed in the text. Generalized surface geology follows the classification of Wills *et al.* (2000): white contains classes B, BC, and C; dark shading is CD; and light shading is class D. The color version of this figure is available only in the electronic edition.

profiles sampled at each of the strong-motion recording sites and also constraining V_{S30} to be 865 m/s. Table 4 lists the Landers region 1D velocity model. High-frequency Q is modeled using equations (14) and (15), with $x = 0.8$, $a = 41$, and $b = 34$.

Figure 15a,b compares observed and simulated ground-velocity waveforms at five selected sites. Broadband motions are shown in Figure 15a, and low-pass filtered ($f < 0.5$ Hz) records are shown in Figure 15b. These sites are indicated on the map shown in Figure 13 and were chosen as a representative sample spanning the region covered by the simulation. Because we are using a generalized rupture model of this earthquake that incorporates only limited information about the actual rupture, we cannot hope to match all the details of the recorded waveforms. As with the previous simulations, the amplitude, duration, and frequency content of the observed waveforms are matched reasonably well by the simulation for these sites. Due to primarily unilateral rupture initiating at the southern end of the fault, the Landers event produced strong rupture directivity effects toward the northwest. These effects are readily seen in the observed and simulated waveforms at stations LUC and CE23559. Station LUC is very close to the rupture; the motions here are concentrated into brief pulselike arrivals, which are strongest on the fault-normal (240° azimuth) horizontal

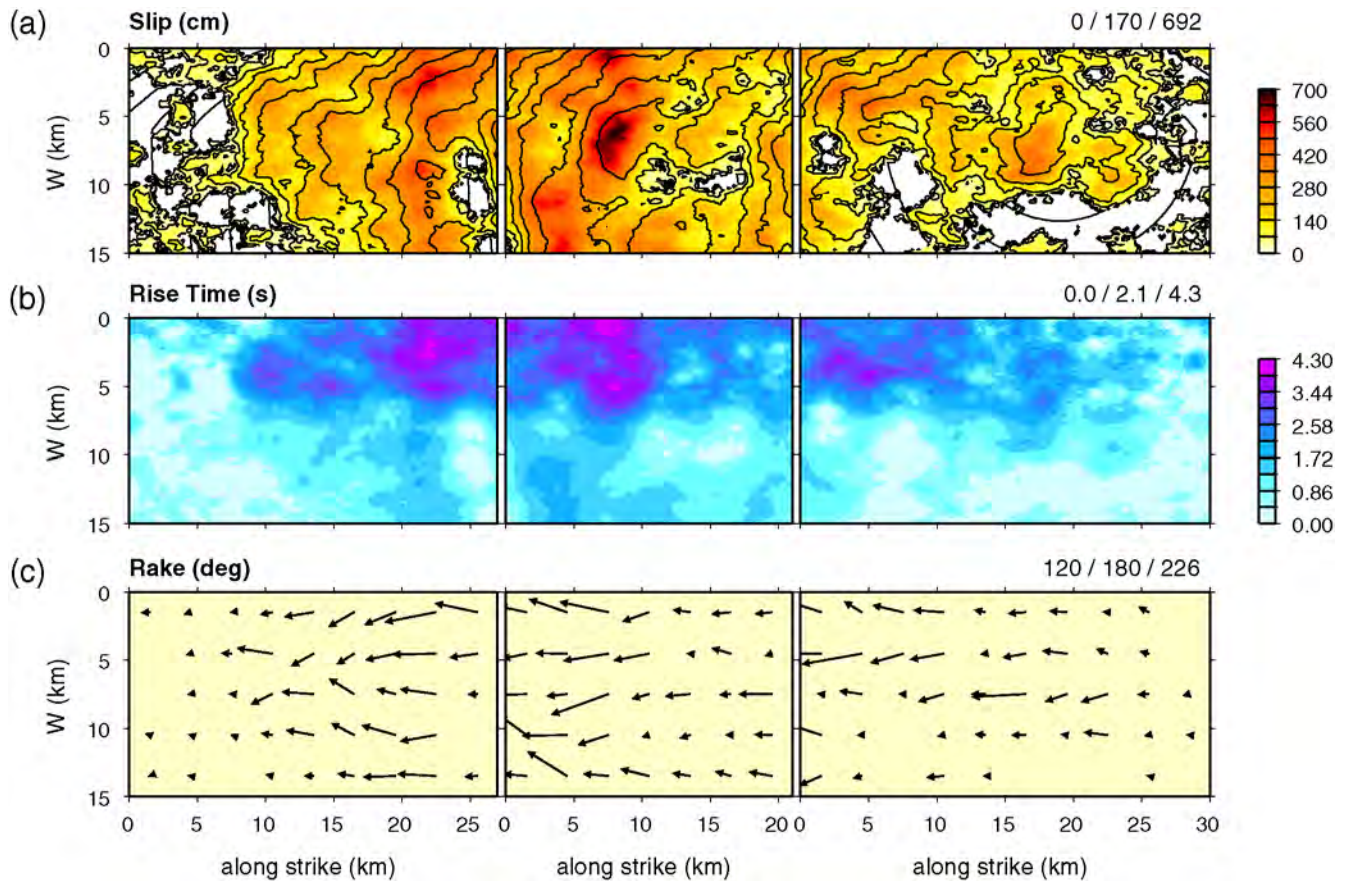


Figure 14. Kinematic rupture description developed for the three segment model of the Landers earthquake. (a) Panel shows slip distribution with rupture front contours at 1 s intervals super imposed, (b) panel shows distribution of slip rise time, and (c) panel shows distribution of rake. Triplet of numbers at top right of each panel indicates the minimum, mean, and maximum values of the given distribution, respectively. The color version of this figure is available only in the electronic edition.

component. The simulated motions at LUC exhibit somewhat more complexity than the observed waveforms, probably related to inadequacies in our assumed rupture model. At the more distant station CE23559, the waves begin to disperse due to developing surface wave energy; however, the effects of rupture directivity are still apparent with the fault-normal motions having twice the amplitude of the fault-parallel motions (150° azimuth). For the sites located off the sides of the fault (CE23583 and CE21081), the observed and simulated waveforms are characterized by a series of relatively longer period arrivals and somewhat stronger fault-parallel motions compared with the fault-normal motions. These sites experience a much longer apparent source duration relative to the more northern sites, which leads to the extended series of arrivals with the motions more strongly polarized on the fault-parallel component due to the predominantly strike-slip nature of the rupture. Near the epicenter (5071), the amplitude of motion is relatively low and the duration of shaking is much longer compared with the sites to the north. These features result from the rupture propagating away from this site, giving rise to a very long apparent source duration even though the site is relatively close to the rupture.

Figure 16 compares observed and simulated PGA and PGV as functions of closest distance to the rupture surface. Both the level and trend of the observations are matched quite

Table 4
Landers Region 1D Velocity Profile

Thickness (km)	V_p (km/s)	V_s (km/s)	Density (g/cm ³)
0.002	1.70	0.45	2.00
0.004	1.80	0.65	2.10
0.006	1.80	0.85	2.10
0.008	1.90	0.95	2.10
0.01	2.00	1.15	2.20
0.07	2.80	1.40	2.30
0.20	3.40	1.70	2.40
0.20	3.90	2.00	2.50
0.20	4.30	2.30	2.60
0.30	4.40	2.50	2.65
2.00	5.10	2.80	2.70
2.00	6.00	3.30	2.75
1.00	6.10	3.45	2.80
5.00	6.15	3.60	2.825
5.00	6.32	3.65	2.85
5.00	6.55	3.70	2.90
10.00	6.80	3.80	2.95
–	7.80	4.50	3.20

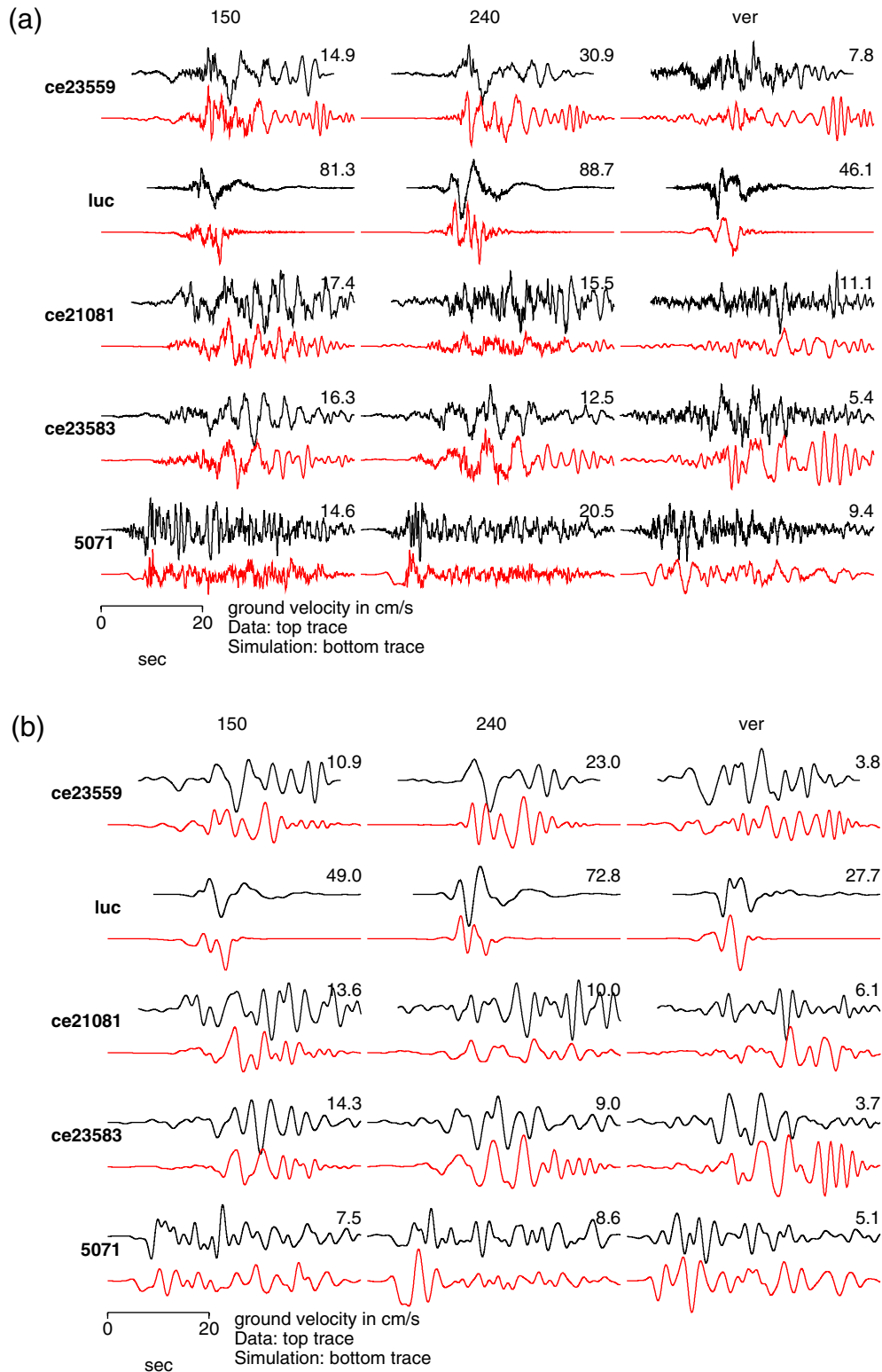


Figure 15. (a) Comparison of recorded (top) and simulated (bottom) broadband three-component ground-velocity waveforms at five selected sites for the Landers earthquake. Horizontal components have been rotated into fault-parallel (150° azimuth) and fault-normal (240° azimuth) orientations. Station locations are indicated in Figure 13. The recorded and simulated motions for each component and station are scaled to the maximum value listed above each pair of waveforms. (b) Comparison of recorded (top) and simulated (bottom) low-pass filtered ($f < 0.5$ Hz) three-component ground-velocity waveforms at five selected sites for the Landers earthquake. Horizontal components have been rotated into fault-parallel (150° azimuth) and fault-normal (240° azimuth) orientations. Station locations are indicated in Figure 13. The recorded and simulated motions for each component and station are scaled to the maximum value listed above each pair of waveforms. The color version of this figure is available only in the electronic edition.

well by the simulation. In contrast to the other simulations, the amount of variability produced by the simulation is about the same as observed for both PGA and PGV. The apparent increase in simulated high-frequency variability may, to certain extent, result from the relatively sparse and geographically distributed set of stations that are available for the Landers earthquake. The residuals shown in Figure 16b,d show little systematic bias either as functions of distance or site type. Additionally, a similar result is found for 5% damped spectral acceleration at periods ranging from 0.05 to 5 s (see the [E](#) electronic supplement to this paper).

Using equations (19), (20), and (21), we compute the model bias and standard error for 5% damped spectral acceleration over a suite of periods from 0.05 to 8 s for the Landers simulation. The results are displayed in Figure 17 for the fault-parallel (150° azimuth), fault-normal (240° azimuth), and average horizontal (geometric mean) components. This comparison is limited to sites having a closest distance within 80 km from the rupture, yielding a total of 21 sites. The model bias is near zero for all components across the entire bandwidth indicating that, on average, the simulation is accurately reproducing the main characteristics of the observed ground motions. The standard error for these comparisons is about 0.4 to 0.5 natural log units for periods less than about

0.5 s. For periods longer than 0.5 s, the standard error increases to about 0.6 to 0.7 natural log units. The increased standard error at the longer periods is probably due to deficiencies in our assumed rupture model, which have a relatively stronger impact on the deterministic aspects of the simulation.

1979 Imperial Valley Earthquake

Our model region for the 1979 Imperial Valley earthquake covers the area within about 60 km of the rupture surface, which includes 33 strong-motion recording sites. A detailed listing of these sites is given in the [E](#) electronic supplement to this paper. Figure 18 shows a map view of the rupture plane and recording sites. The site types are primarily CD and D (Wills *et al.*, 2000). We have adopted a fault geometry and hypocenter following Hartzell and Heaton (1983) for our simulations. We do not consider rupture on the adjacent Brawley fault, as this contributes only a small fraction of the total moment release (Olson and Apsel, 1982; Archuleta, 1984). Our fault model has a length of 39 km, a down-dip width of 10.5 km, a strike of 143°, and a dip of 90°. This model deviates slightly from the Hartzell and Heaton (1983) representation in that we have trimmed 3 km from the northwestern end of their fault

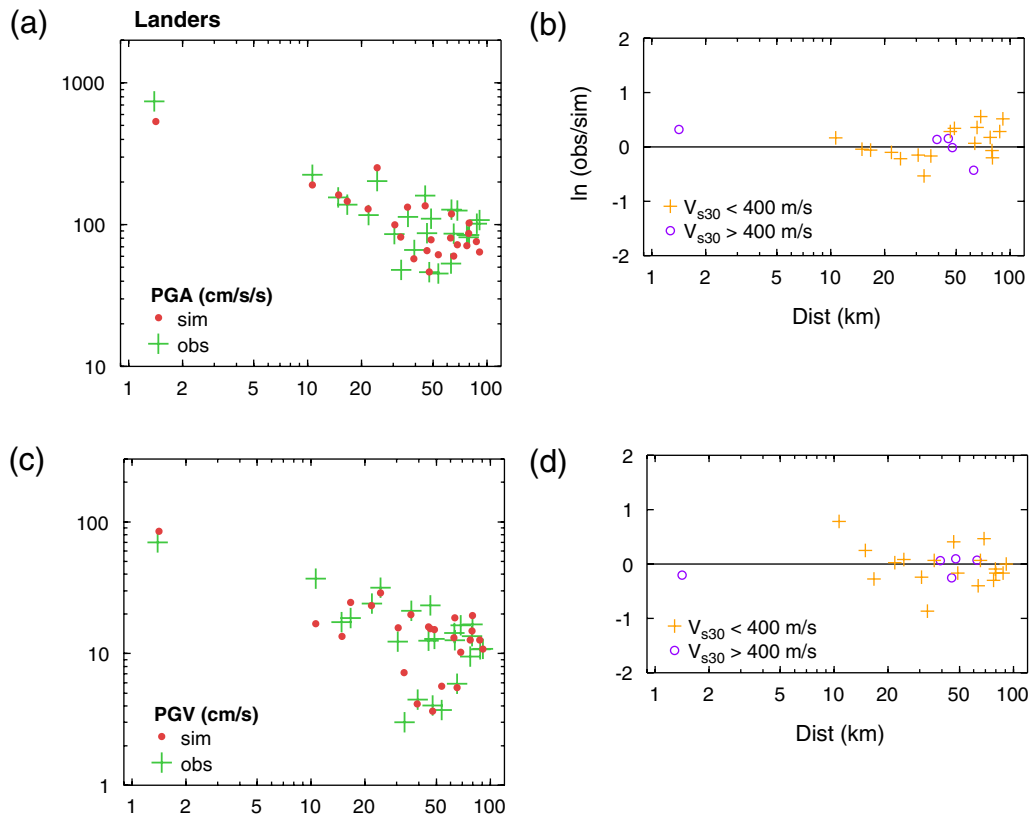


Figure 16. (a), (b) Comparison of recorded and simulated PGA (left) and (c), (d) PGV (right) plotted as functions of closest distance to the fault surface for the Landers earthquake. (a), (c) Top panels show absolute ground-motion values (recorded as crosses, simulated as circles) and (b), (d) panels show the residuals of the recorded and simulated values in natural log units. For residuals, sites have been separated into two groups based on V_{s30} . The color version of this figure is available only in the electronic edition.

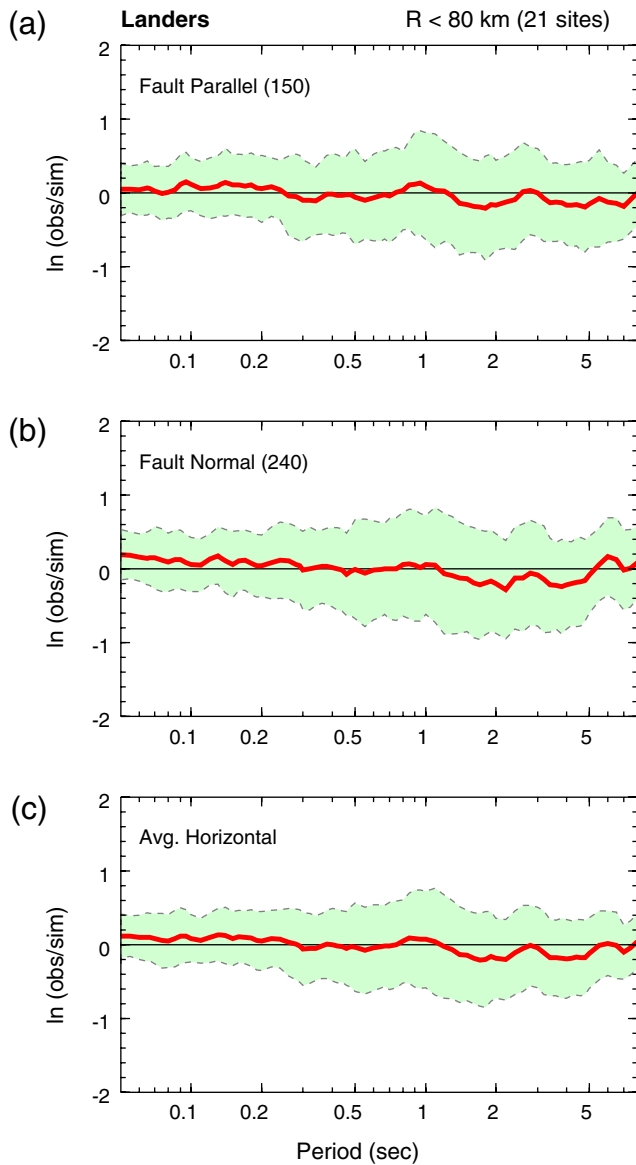


Figure 17. Model bias (heavy line) and standard error (shaded region) for 5% damped spectral acceleration using 21 sites for the Landers earthquake. (a) Panel is for fault-parallel component, (b) panel is for fault-normal component, and (c) panel is for the average horizontal (geometric mean) component. The color version of this figure is available only in the electronic edition.

because the slip is essentially zero in this section. The average rake is 180° . Table 1 lists the fault parameters used for our rupture model. We use a seismic moment of 6.02×10^{25} dyne-cm, giving a moment magnitude of 6.49.

The derivation of our rupture model starts from a low-pass version of the Hartzell and Heaton (1983) slip distribution, and then we generate the full kinematic description using the steps described earlier. Figure 19 displays the rupture model developed for our simulations. Because the rupture is confined to depths shallower than about 10 km, the decrease of the rupture propagation speed and the lengthening of the rise time within the upper 5 km are quite signifi-

cant. In particular, the strong refraction of the rupture front in the shallow portion of the fault bends the propagation direction toward the vertical and produces a very high apparent propagation speed at the ground surface. Locally, the rupture speed exceeds the shear-wave velocity only in the deeper high slip portions of the fault, which is consistent with some previous models of this earthquake (e.g., Archuleta, 1984).

The subsurface velocity structure is based on the SCEC CVM4, modified to include the Boore and Joyner (1997) generic rock velocity structure in the near surface of the non-basin portions of the model. In addition, we have replaced the CVM4 shear-wave velocities within the Imperial Valley sediment using the mudline relation of Brocher (2005). This was necessary because the lowest shear-wave velocity for these sediments in the original CVM4 is unrealistically high (about 800 m/s). For the low-frequency simulation, we discretize the model at a uniform grid spacing of 0.1 km and impose a minimum shear-wave velocity threshold of 0.5 km/s. For the high-frequency simulation, we construct a representative 1D velocity profile by averaging the profiles sampled at each of the strong-motion recording sites and also constraining V_{S30} to be 865 m/s. Table 5 lists the Imperial Valley region 1D velocity model. High-frequency Q is modeled using equations (14) and (15), with $x = 0.8$, $a = 8$, and $b = 20$.

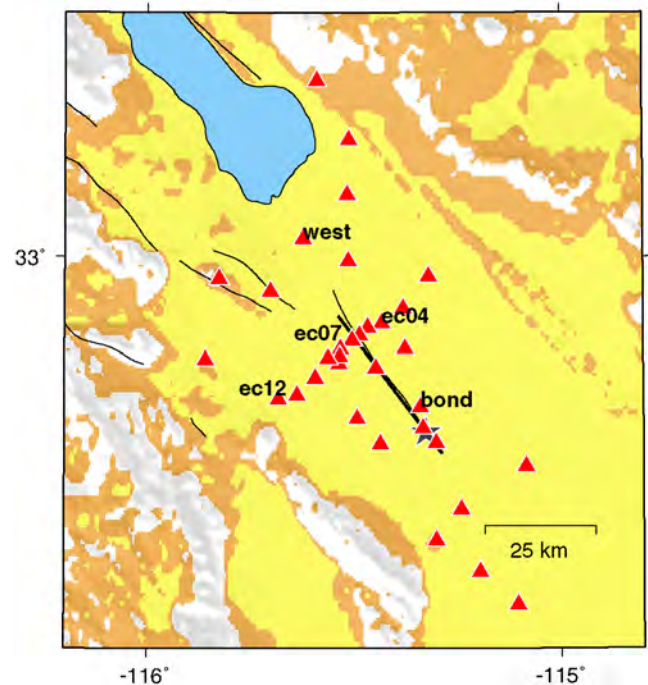


Figure 18. Map of the model region used for the 1979 Imperial Valley earthquake simulation. The heavy line indicates the surface fault trace. The star is the epicenter and the triangles are recording stations analyzed in our study. Labeled stations are discussed in the text. Generalized surface geology follows the classification of Wills *et al.* (2000): white contains classes B, BC, and C; dark shading is CD; and light shading is class D. The color version of this figure is available only in the electronic edition.

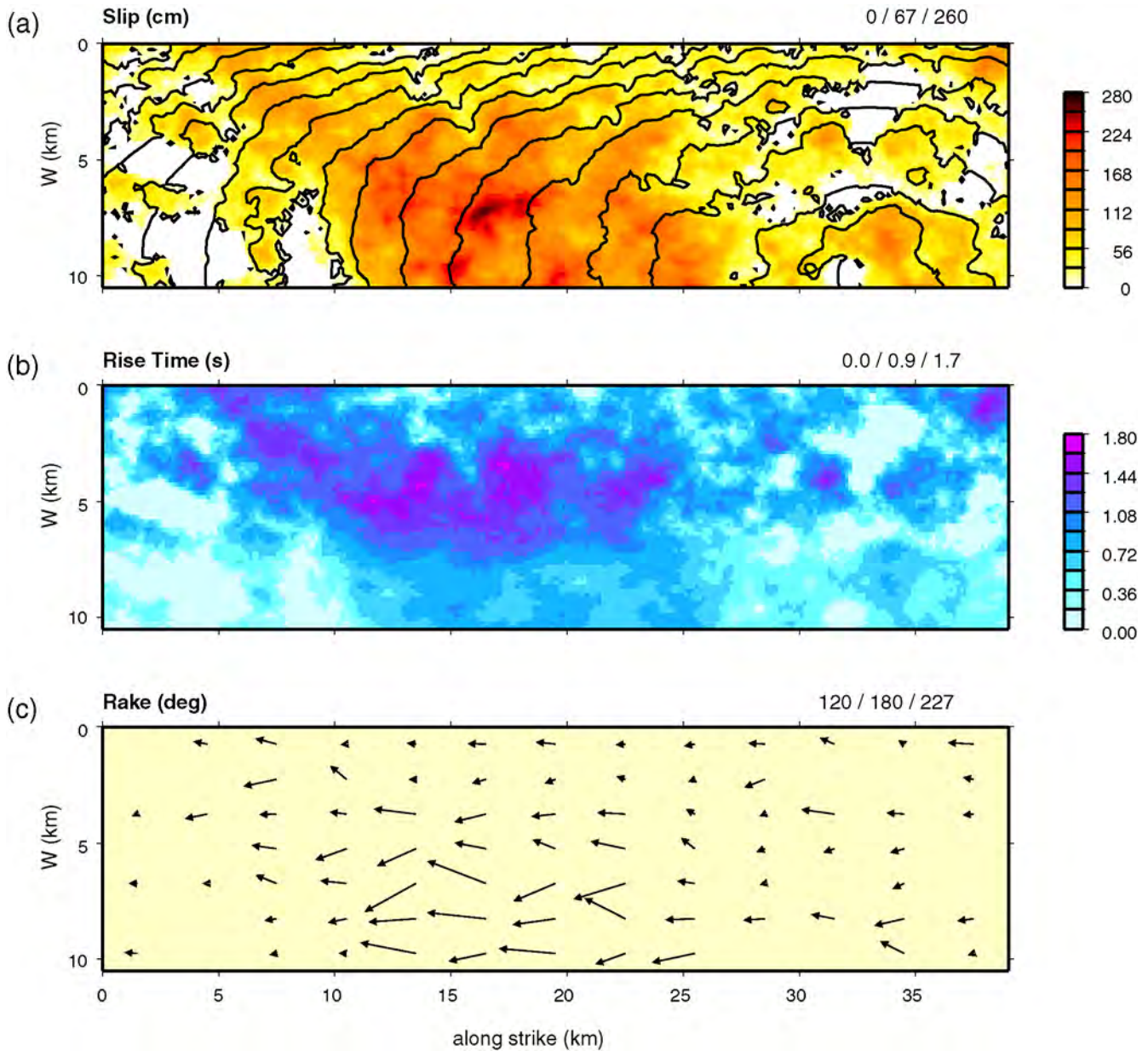


Figure 19. Kinematic rupture model developed for the 1979 Imperial Valley earthquake. (a) Panel shows slip distribution with rupture front contours at 1 s intervals super imposed, (b) panel shows distribution of slip rise time, and (c) panel shows distribution of rake. Triplet of numbers at top right of each panel indicates the minimum, mean and maximum values of the given distribution, respectively. The color version of this figure is available only in the electronic edition.

Observed and simulated ground-velocity waveforms at five selected sites are compared in Figure 20a,b. Broadband motions are shown in Figure 20a, and low-pass filtered ($f < 0.5$ Hz) records are shown in Figure 20b. These sites are indicated on the map shown in Figure 18 and were chosen as a representative sample spanning the region covered by the simulation. Because we are using a generalized rupture model of this earthquake that incorporates only limited information about the actual rupture, we cannot hope to match all the details of the recorded waveforms. As with the previous simulations, the amplitude, duration, and frequency content of the observed waveforms are matched rea-

sonably well by the simulation for all these sites. The station at BOND is located near the epicenter at a distance of 2.5 km from the rupture plane. The motions at this site are relatively strong (PGV of 53 cm/s) and are characterized by a sequence of higher frequency arrivals lasting about 8 to 10 s. Because this site is located close to the epicenter, it experiences a relatively long apparent source duration as the rupture propagates away from the site. Both the amplitude and character of the observed waveforms are matched well by the simulation.

As was observed with Landers, the Imperial Valley event produced strong rupture directivity effects toward

Table 5
Imperial Valley Region 1D Velocity Profile

Thickness (km)	V_p (km/s)	V_s (km/s)	Density (g/cm ³)
0.002	1.70	0.45	2.00
0.004	1.80	0.65	2.10
0.006	1.80	0.85	2.10
0.008	1.90	0.95	2.10
0.01	2.00	1.15	2.20
0.07	2.40	1.20	2.20
0.20	2.50	1.25	2.30
0.20	2.60	1.30	2.30
0.20	2.80	1.40	2.35
0.30	2.90	1.50	2.40
0.50	3.00	1.60	2.45
0.50	3.40	1.90	2.50
0.50	3.90	2.20	2.55
0.50	4.20	2.40	2.60
2.00	5.00	2.90	2.65
1.00	5.30	3.00	2.70
2.50	5.45	3.15	2.75
2.50	6.00	3.40	2.80
5.00	6.60	3.65	2.95
6.00	7.30	4.10	3.00
9.00	7.50	4.30	3.05
–	7.80	4.50	3.20

the northwest due to primarily unilateral rupture initiating at the southern end of the fault. These effects are readily seen in the observed and simulated waveforms at stations EC07 and EC04, which are located 0.9 and 6.9 km from the rupture plane, respectively. The motions at both of these sites are concentrated into brief pulslike arrivals, with the observed fault-normal (233° azimuth) horizontal component having roughly twice the amplitude as the observed fault-parallel (143° azimuth) horizontal component. Additionally, the horizontal motions are much stronger than the vertical motions. These characteristics are matched well by the simulation for all components at EC04. For station EC07, the simulation reproduces the observed waveforms quite nicely; however, it overpredicts the observed fault-normal motions by about a factor of 2 and underpredicts the observed vertical motions by roughly the same factor. Because this site is virtually on top of the rupture plane, the amplitudes of the motions are quite sensitive to small changes in both the orientation (i.e., strike, dip, and rake) of the rupture (e.g., [Hartzell and Heaton, 1983](#)), as well as the local rupture speed (e.g., [Archuleta, 1984](#)). Thus, allowing the rupture surface to deviate from the purely vertical plane assumed in our model or allowing for different rupture speed variations than predicted by our assumed scaling relations may improve the amplitude fit at this site.

With increasing distance from the fault, the waves begin to disperse due to developing surface wave energy within the sediments of the Imperial basin. At station WEST, the effects of rupture directivity are still evident with the observed fault-normal motions having about twice the amplitude of the observed fault-parallel motions. The simulation reproduces the observed waveforms reasonably well at this site, but it over-

predicts the amplitude of the fault-normal motions, particularly for the later arriving energy. This may be due to deficiencies in the assumed rupture model, as discussed previously, possibly coupled with deficiencies in the assumed 3D velocity structure. At station EC12, which is located to the west of the fault at a distance of about 18 km, the observed and simulated waveforms are characterized by a series of relatively longer period arrivals having roughly equal fault-parallel and fault-normal motions.

Figure 21 compares observed and simulated PGA and PGV as functions of closest distance to the rupture surface. Overall, the level and trend of the observations are matched reasonably well by the simulation. For distances less than about 20 km, the amount of variability produced by the simulation is about the same as observed for both PGA and PGV. For greater distances, the simulation tends to underpredict the observed level of variability. The residuals shown in Figure 21b,d show a slight trend of overprediction at very close distances (<2 km) and underprediction at larger distances (>30 km). A similar result is found for 5% damped spectral acceleration at periods ranging from 0.05 to 5 s (see the [E](#) electronic supplement to this paper). For the near-fault sites, we suspect the overprediction results from incomplete characterization of nonlinear effects by the approximate site response factors used in our simulation. The underprediction at the more distant sites is probably related to inadequacies in the 3D velocity model or our assumed anelastic attenuation function.

Using equations (19), (20), and (21), we compute the model bias and standard error for 5% damped spectral acceleration over a suite of periods from 0.05 to 8 s for the Imperial Valley simulation. The results are displayed in Figure 22 for the fault-parallel (143° azimuth), fault-normal (233° azimuth), and average horizontal (geometric mean) components. This comparison is limited to sites having a closest distance within 40 km from the rupture, yielding a total of 31 sites. The model bias is near zero for all components across the entire bandwidth indicating that, on average, the simulation is reproducing the main characteristics of the observed ground motions. There is a slight trend for underprediction of fault-parallel and overprediction of fault-normal motions for periods around 1 to 2 s, suggesting that the effects of rupture directivity may be over estimated by our model. The standard error for these comparisons is about 0.7 to 0.8 natural log units.

Discussion and Conclusion

Figure 23 summarizes the spectral acceleration modeling bias (from equation 20) for the four earthquakes we have examined, along with corresponding measures computed from the four NGA GMPEs ([Abrahamson and Silva, 2008](#); [Boore and Atkinson, 2008](#); [Campbell and Bozorgnia, 2008](#); [Chiou and Youngs, 2008](#)). For all four events, the simulations have a model bias generally within 20% of zero across the full bandwidth. Of the events we consider, two are buried

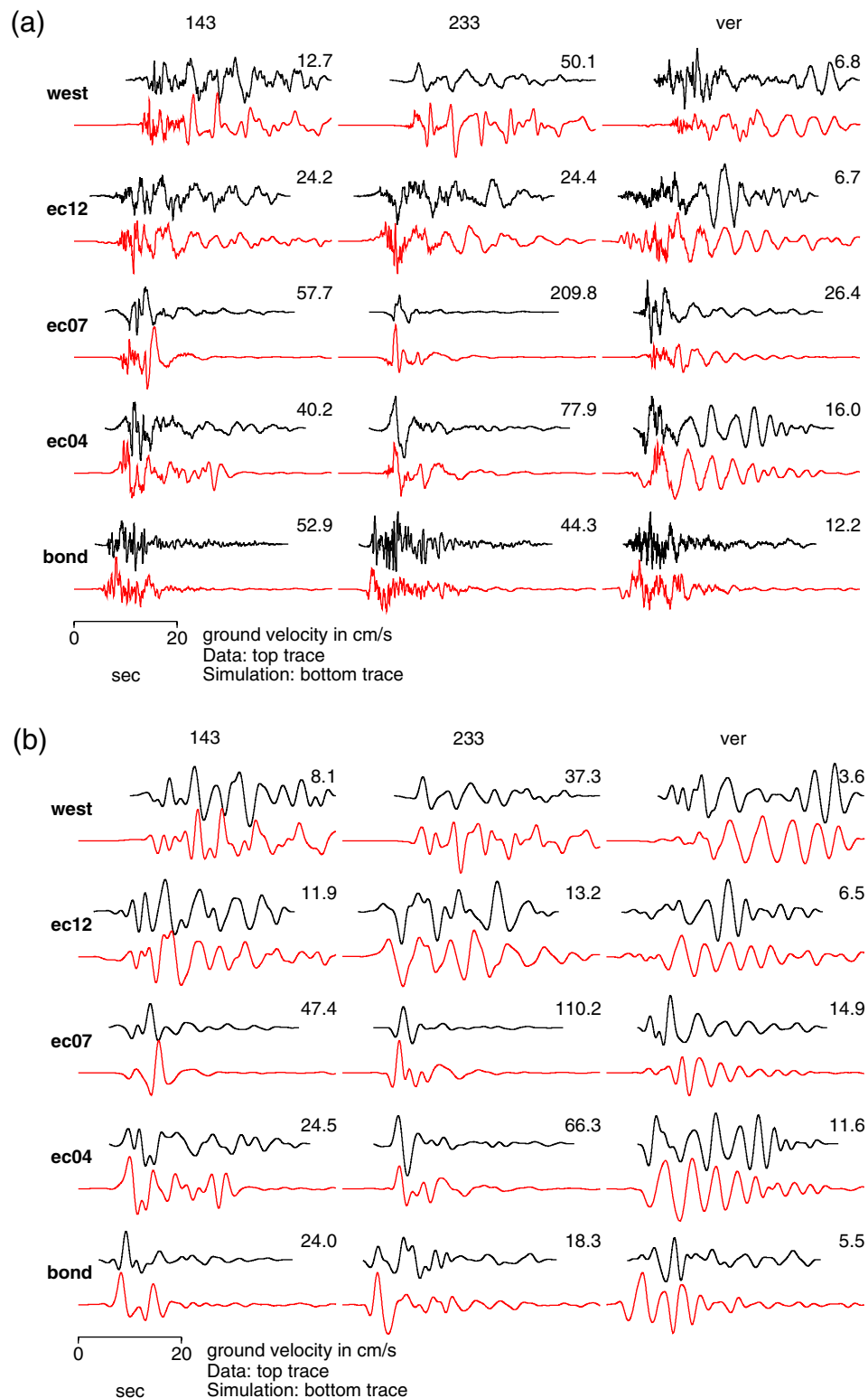


Figure 20. (a) Comparison of recorded (top) and simulated (bottom) broadband three-component ground-velocity waveforms at five selected sites for the 1979 Imperial Valley earthquake. Horizontal components have been rotated into fault-parallel (143° azimuth) and fault-normal (233° azimuth) orientations. Station locations are indicated in Figure 18. The recorded and simulated motions for each component and station are scaled to the maximum value listed above each pair of waveforms. (b) Comparison of recorded (top) and simulated (bottom) low-pass filtered ($f < 0.5$ Hz) three-component ground-velocity waveforms at five selected sites for the 1979 Imperial Valley earthquake. Horizontal components have been rotated into fault-parallel (143° azimuth) and fault-normal (233° azimuth) orientations. Station locations are indicated in Figure 18. The recorded and simulated motions for each component and station are scaled to the maximum value listed above each pair of waveforms. The color version of this figure is available only in the electronic edition.

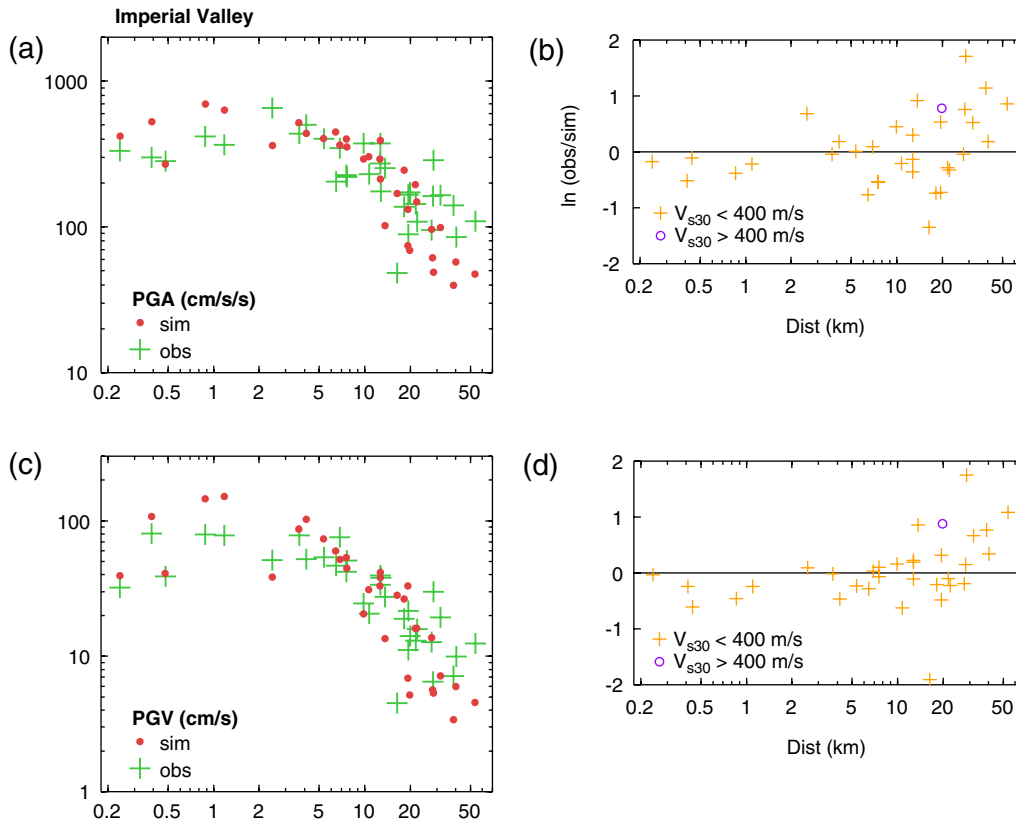


Figure 21. (a), (b) Comparison of recorded and simulated PGA (left) and (c), (d) PGV (right) plotted as functions of closest distance to the fault surface for the 1979 Imperial Valley earthquake. (a), (c) Panels show absolute ground-motion values (recorded as crosses, simulated as circles) and (b), (d) panels show the residuals of the recorded and simulated values in natural log units. For residuals, sites have been separated into two groups based on V_{s30} . The color version of this figure is available only in the electronic edition.

ruptures (Loma Prieta and Northridge) and two are surface ruptures (Imperial Valley and Landers). For the surface rupturing events, the model bias from our simulations and the GMPEs are quite similar for periods less than about 1 s, whereas at periods above 1 s the GMPEs begin to diverge. For Imperial Valley, AS08 and BA08 trend to a positive bias (underprediction), while CB08 and CY08 remain near zero; and for Landers, AS08 and CY08 trend to a positive bias, while BA08 and CB08 remain near zero. On the contrary, for the buried rupture events, all of the GMPEs have a systematic and significant positive bias ranging from about 20 to 60% over a wide portion of the period band.

The relative increase of ground-motion levels for buried versus surface ruptures has been documented in several earthquakes (e.g., Kagawa *et al.*, 2004) and has also been examined using dynamic rupture models that include a shallow weak zone (e.g., Dalguer *et al.*, 2008; Pitarka *et al.*, 2009). We model these effects in our simulations with depth-dependent scaling of rise time, rupture speed, and corner frequency. This provides a physical basis for reproducing the observed ground-motion differences between buried and surface rupturing events, and the results shown in Figure 23 lend support to this approach. The GMPEs address these effects using regression terms generally conditioned on the depth to top of rupture; however, the specific implementation

and resulting behavior vary considerably from relation to relation (see Abrahamson *et al.*, 2008). The results shown in Figure 23 suggest that this simplified approach may not capture the full extent of these effects, at least for the events studied here.

Figure 24 summarizes the modeling standard error for spectral acceleration (from equation 21) for the four earthquakes we have examined along with corresponding measures computed from the four NGA GMPEs. For Loma Prieta and Northridge, the simulations and GMPEs produce very similar results, with standard errors generally around 0.5 (natural log units) across most of the period band considered. For both surface rupturing events, the GMPEs produce very consistent results, with standard errors around 0.5 at short periods, which then increase to about 0.8 at longer periods. However, the simulations for these events exhibit noticeably different behavior. For Landers, the simulation has a low standard error of about 0.3 at short periods, which then increases to about 0.7 around 1 s period before decreasing again at longer periods. For Imperial Valley, the standard error for the simulation is systematically high at about 0.7 to 0.8 for all periods. We suspect that these differences primarily reflect the relative complexity of the regional velocity structures where these two events occurred, as well as our level of knowledge about these structures and how to incorporate them in our

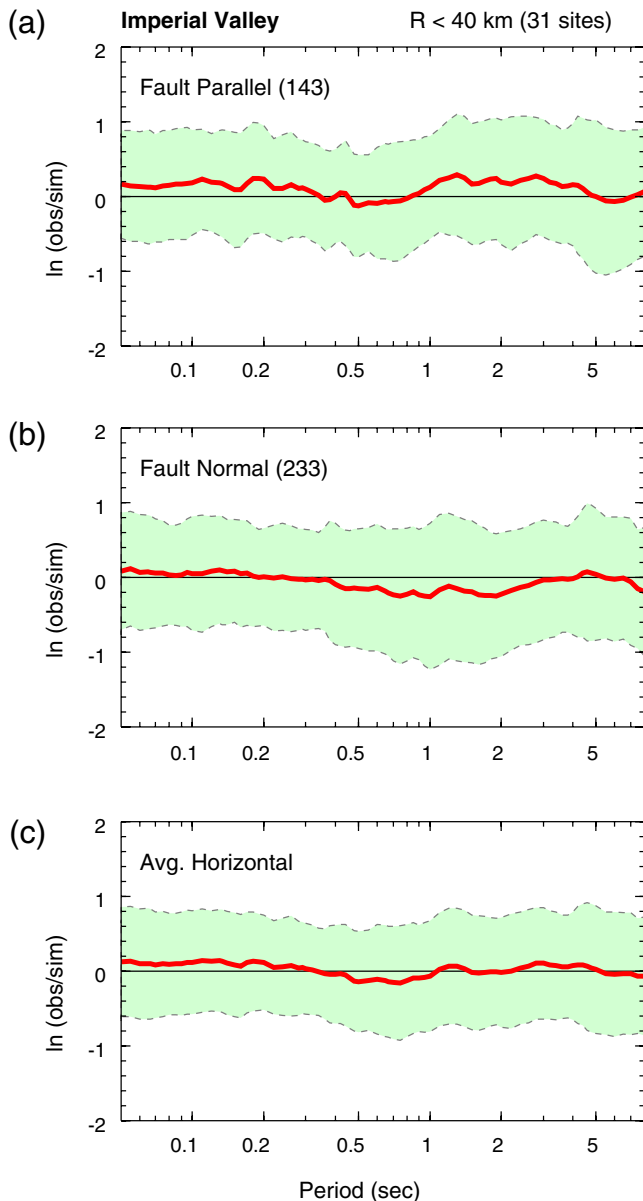


Figure 22. Model bias (heavy line) and standard error (shaded region) for 5% damped spectral acceleration using 31 sites for the 1979 Imperial Valley earthquake. (a) Panel is for fault-parallel component, (b) panel is for fault-normal component, and (c) panel is for the average horizontal (geometric mean) component. The color version of this figure is available only in the electronic edition.

simulations. Landers occurred in the Mojave region, which is characterized by shallow sediment accumulations and predominantly 1D crustal velocity variations that are represented reasonably well by the tomography model (Hauksson and Haase, 1997), incorporated in the SCEC CVM4. Consequently, the propagation and site response effects are modeled reasonably well by the simulation approach. On the other hand, the Imperial Valley event occurred within a deep sedimentary basin that is currently not well constrained in the SCEC CVM4. As we have already discussed, much of the scatter in our modeling of the Imperial Valley event can be explained by

a trend of overprediction at close distance and underprediction at larger distance, which is suggestive of deficiencies in our path and site response characterization. Currently, studies are underway to develop a better understanding of the velocity structure throughout the Imperial Valley region (Hole *et al.*, 2009); this should improve our ability to model these earthquake ground motions.

In the process of developing the rupture models used for our simulations, we have found that while our seismic moments fall within the range of reported values, they tend to be somewhat lower than the average of estimates provided in other studies. We suspect the reasons for this are twofold. First, the inclusion of site-specific amplification factors in our methodology tends to amplify the motions on softer soil sites, which requires less source-radiated energy to match the observed level of shaking. Typically, source inversion studies do not utilize these types of factors; in many cases, these studies have used relatively high near surface shear-wave velocities for the calculation of Green's functions (e.g., Wald and Heaton, 1994). The second reason is related to the bandwidth over which the strong ground motions that we model are most concentrated, which is about 0.1 to 10 Hz. Extending on earlier work by Das (1982), recent studies (e.g., King and Wesnousky, 2007; Shaw and Wesnousky, 2008) suggest that a substantial portion of coseismic moment release during large crustal earthquakes may occur beneath the seismogenic layer with relatively long rise times and a depletion of radiated high-frequency energy. This moment release would not significantly contribute to the strong ground-motion response, but it may be detected by lower frequency analyses utilizing teleseismic and/or geodetic observations.

Because our simulation methodology produces broadband time series, the resulting ground motions can be utilized in many different ways. An example of this is shown in Figure 25, which compares ground-motion ShakeMaps (Wald *et al.*, 1999; Wald *et al.*, 2005) computed from our simulations with those computed from the USGS observed motions for the Loma Prieta earthquake (see the Data and Resources section). In order to compute a simulated ShakeMap, we first calculate broadband waveforms on a dense grid of points (typically 1 to 2 km spacing) covering the region of interest. From these waveforms, we can then extract various intensity measures including PGA, PGV, spectral acceleration, and instrumental intensity (MMI). Wald *et al.* (1999) and Wald *et al.* (2005) provide quantitative relationships to compute MMI from PGA and PGV. The comparison in Figure 25 demonstrates that the simulated ShakeMaps are able to capture many of the features seen in the observed motions. Additional ShakeMap comparisons for the other events we have modeled are included in the [E](#) electronic supplement to this paper. These ShakeMaps also highlight the predictive capability of the simulation approach. Using the methodology presented here, it is straightforward to generate ShakeMaps for scenario earthquakes that can be used for planning and preparedness activities, as was recently done for the Hayward fault in northern California (Aagaard,

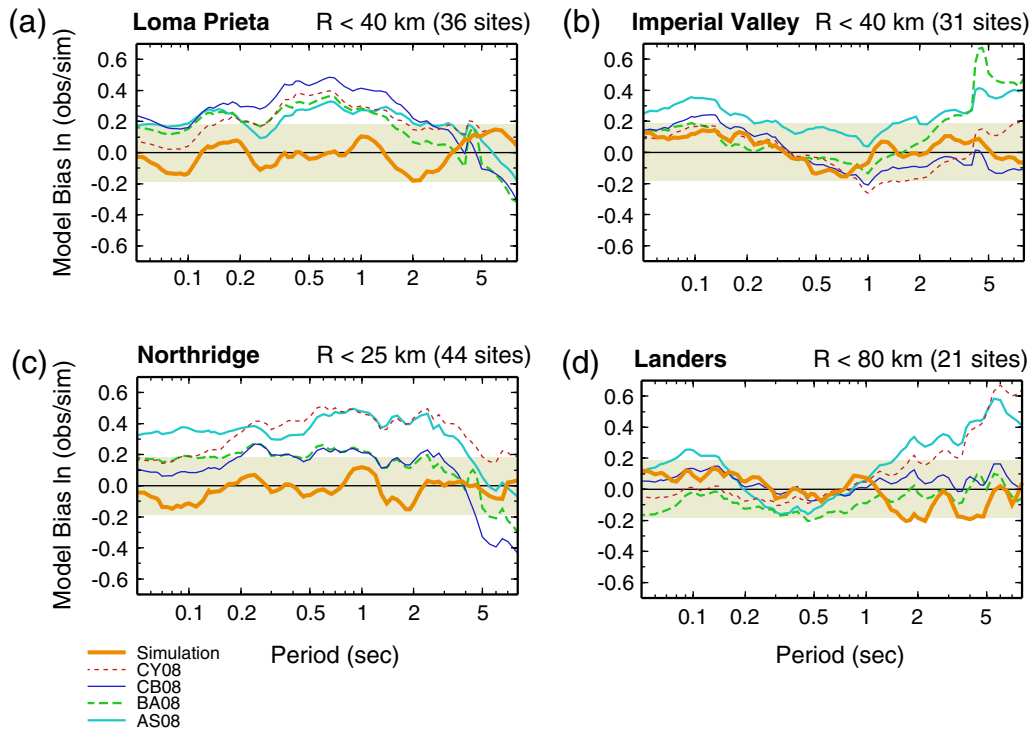


Figure 23. Comparison of spectral acceleration modeling bias from our simulations with that obtained from four NGA GMPEs for near-fault sites of studied events. Shaded region represents range of $\pm 20\%$ about zero bias. Distance range and number of sites considered for each event is listed at top right of each panel. The color version of this figure is available only in the electronic edition.

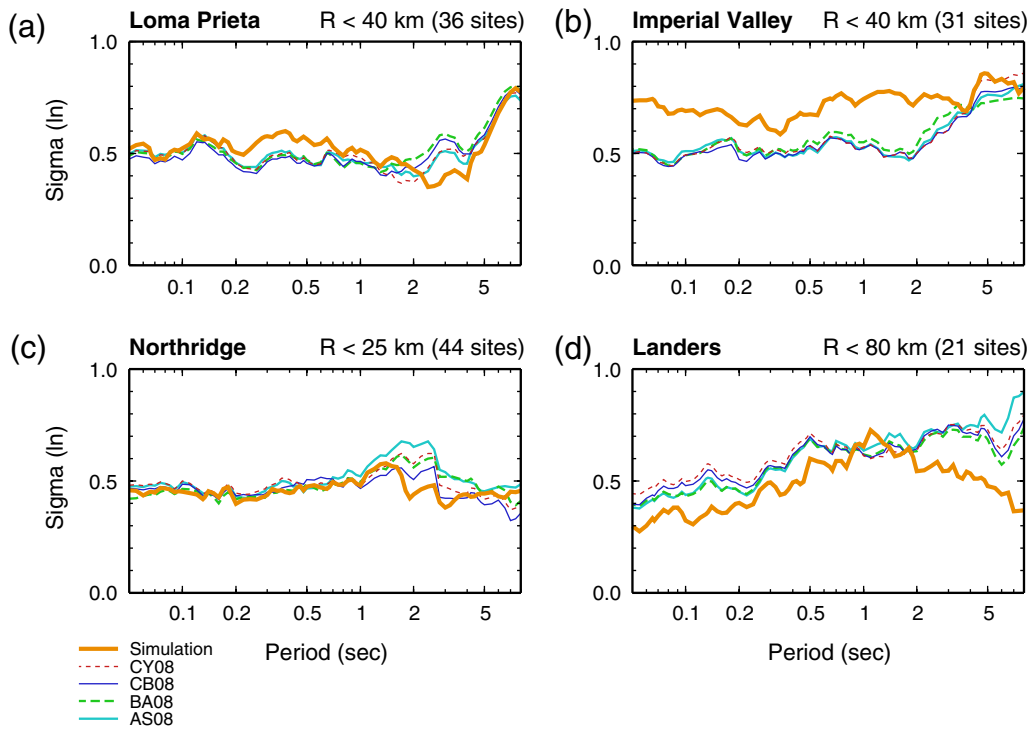


Figure 24. Comparison of spectral acceleration standard error for our simulations with that obtained from four NGA GMPEs for near-fault sites of studied events. Distance range and number of sites considered for each event is listed at top right of each panel. The color version of this figure is available only in the electronic edition.

Graves, Schwartz *et al.*, 2010) and the San Andreas fault in southern California (Graves *et al.*, 2010).

Our analysis here must be viewed in the proper context. We have examined four crustal earthquakes occurring within one active tectonic region. Additional investigation is required to test the applicability of our approach to other active tectonic regions (e.g., Japan) or other tectonic regimes (e.g., stable continents). This is the subject of continuing research. While the ultimate goal of the simulation methodology is to deterministically reproduce observed waveforms and ampli-

tudes at frequencies up to several Hz or more, this is currently only realizable for frequencies less than about 0.5 Hz, even under the best conditions (e.g., Graves, 2008). At higher frequencies, the character of the motions is more stochastic in nature, and our understanding of source and wave propagation phenomena is much less well constrained. Hence, the inclusion of stochastic features within the simulation approach provides a viable means of modeling these higher frequency effects. Within this context, the validation results presented here demonstrate the ability of the hybrid

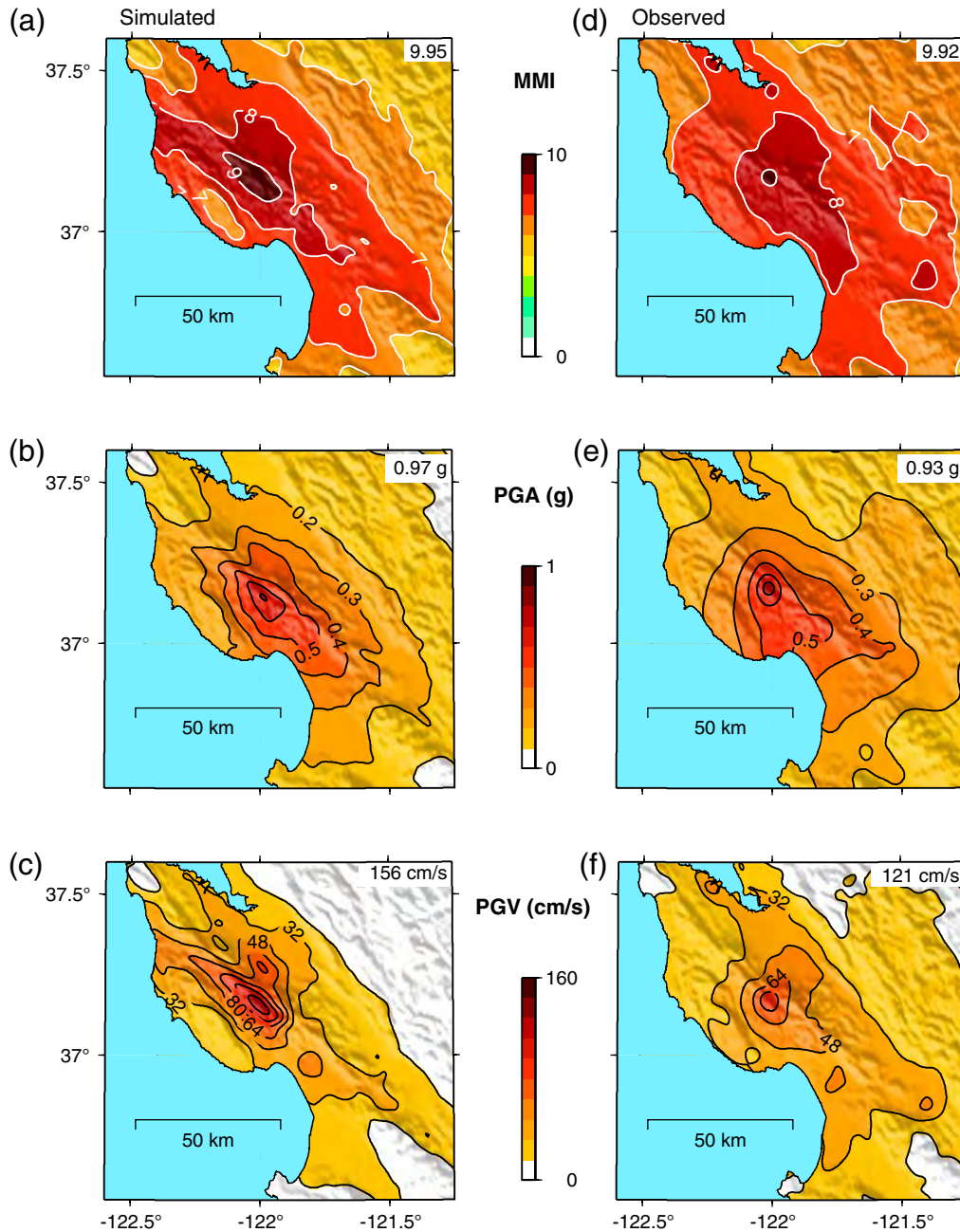
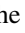


Figure 25. (a), (b), (c) Comparison of simulated (left) and (d), (e), (f) observed (right) ShakeMaps for Loma Prieta earthquake. (a), (d) Top row is instrumental intensity (MMI), (b), (e) middle is peak ground acceleration (PGA), and (c), (f) bottom is peak ground velocity (PGV). The color version of this figure is available only in the electronic edition.

simulation methodology to reproduce the main characteristics of the observed near-fault ground motions for crustal earthquakes over a broad frequency range.

Data and Resources

The ground-motion waveform data used in this paper were obtained from the PEER/NGA strong-motion database (<http://peer.berkeley.edu/nga>, last accessed July 2010) and the Center for Engineering Strong Motion Data (www.strongmotioncenter.org, last accessed July 2010). The  electronic supplement contains detailed listings of recording stations, archives of simulated and recorded broadband waveforms, supplementary plots including simulated and observed ShakeMaps, data files of the kinematic rupture models, and movies of rupture evolution and wave-field propagation for each of the studied earthquakes. All figures in the paper were generated using GMT version 4.2.1 (www.soest.hawaii.edu/gmt, last accessed July 2010; Wessel and Smith, 1998). The subsurface velocity structure based on version 08.3.0 of the USGS 3D Bay Area Velocity Model is found at <http://earthquake.usgs.gov/regional/nca/3Dgeologic> (last accessed July 2010). The subsurface velocity structure based on version 4 of the SCEC CVM4 is found at www.data.scec.org/3Dvelocity (last accessed July 2010). The USGS observed motions for the Loma Prieta earthquake are found at <http://earthquake.usgs.gov/eqcenter/shakemap> (last accessed July 2010).

Acknowledgments

Constructive reviews provided by Art McGarr and two anonymous reviewers were very helpful in revising the paper and making it acceptable for publication. Support for this work was provided by USGS under cooperative agreement 05HQGR0070 and by SCEC under NSF grants EAR-0623704 and OCI-0749313. The large-scale 3D finite-difference simulations were run at USC's Center for High Performance Computing and Communications (www.usc.edu/hpcc, last accessed July 2010) under an agreement with the SCEC Community Modeling Environment project. This is SCEC contribution 1428.

References

- Aagaard, B. T., T. M. Brocher, D. Dolenc, D. Dreger, R. W. Graves, S. Harmsen, S. Hartzell, S. Larsen, K. McCandless, S. Nilsson, N. A. Petersson, A. Rodgers, B. Sjögren, and M. L. Zoback (2008). Ground motion modeling of the 1906 San Francisco earthquake II: Ground motion estimates for the 1906 earthquake and scenario events, *Bull. Seismol. Soc. Am.* **98**, 1012–1046.
- Aagaard, B. T., T. M. Brocher, D. Dolenc, D. Dreger, R. W. Graves, S. Harmsen, S. Hartzell, S. Larsen, and M. L. Zoback (2008). Ground motion modeling of the 1906 San Francisco earthquake I: Validation using the 1989 Loma Prieta earthquake, *Bull. Seismol. Soc. Am.* **98**, 989–1011.
- Aagaard, B. T., R. W. Graves, A. Rodgers, T. M. Brocher, R. W. Simpson, D. Dreger, N. A. Petersson, S. C. Larsen, S. Ma, and R. C. Jachens (2010). Ground motion modeling of Hayward fault scenario earthquakes, Part II: Simulation of long-period and broadband ground motions, *Bull. Seismol. Soc. Am.*, in press.
- Aagaard, B. T., R. W. Graves, D. P. Schwartz, D. A. Ponce, and R. W. Graymer (2010). Ground motion modeling of Hayward fault scenario earthquakes, Part I: Construction of the suite of scenarios, *Bull. Seismol. Soc. Am.*, in press.
- Abrahamson, N., and W. Silva (2008). Summary of the Abrahamson and Silva NGA ground-motion relations, *Earthquake Spectra* **24**, 67–97.
- Abrahamson, N., G. Atkinson, D. Boore, Y. Bozorgnia, K. Campbell, B. Chiou, I. M. Idriss, W. Silva, and R. Youngs (2008). Comparisons of the NGA ground-motion relations, *Earthquake Spectra* **24**, 45–66.
- Anderson, J. G., and S. E. Hough (1984). A model for the shape of the Fourier amplitude spectrum of acceleration at high frequencies, *Bull. Seismol. Soc. Am.* **74**, 1969–1993.
- Archuleta, R. J. (1984). A faulting model for the 1979 Imperial Valley earthquake, *J. Geophys. Res.* **89**, 4559–4585.
- Atkinson, G., K. Assatourians, D. M. Boore, K. Campbell, and D. Motazedian (2009). A guide to difference between stochastic point-source and stochastic finite-fault simulations, *Bull. Seismol. Soc. Am.* **99**, 3192–3201.
- Beresnev, I. A., and G. M. Atkinson (1997). Modeling finite-fault radiation from the ω^n spectrum, *Bull. Seismol. Soc. Am.* **87**, 67–84.
- Beresnev, I. A., and G. M. Atkinson (1998). Stochastic finite-fault modeling of ground motions from the 1994 Northridge, California, earthquake; I. Validation on rock sites, *Bull. Seismol. Soc. Am.* **88**, 1392–1401.
- Boore, D. (2009). Comparing stochastic point-source and finite-source ground motion simulations: SMSIM and EXSIM, *Bull. Seismol. Soc. Am.* **99**, 3202–3216.
- Boore, D. M. (1983). Stochastic simulation of high-frequency ground motions based on seismological models of the radiated spectra, *Bull. Seismol. Soc. Am.* **73**, 1865–1894.
- Boore, D. M., and G. M. Atkinson (2008). Ground-motion prediction equations for the average horizontal component of PGA, PGV, and 5%-damped PSA at spectral periods between 0.01 s and 10.0 s, *Earthquake Spectra* **24**, 99–138.
- Boore, D. M., and W. B. Joyner (1997). Site amplifications for generic rock sites, *Bull. Seismol. Soc. Am.* **87**, 327–341.
- Borcherdt, R. (1994). Estimates of site dependent response spectra for design (methodology and justification), *Earthquake Spectra* **10**, 617–653.
- Brocher, T. M. (2005). Empirical relations between elastic wavespeeds and density in the Earth's crust, *Bull. Seismol. Soc. Am.* **95**, 2081–2092.
- Brune, J. N. (1970). Tectonic stress and spectra of seismic shear waves from earthquakes, *J. Geophys. Res.* **75**, 4997–5009.
- Campbell, K. W., and Y. Bozorgnia (2008). NGA ground motion model for the geometric mean horizontal component of PGA, PGV, PGD and 5% damped linear elastic response spectra for periods ranging from 0.01 to 10 s, *Earthquake Spectra* **24**, 139–172.
- Chiou, B. S. J., and R. R. Youngs (2008). Chiou-Youngs NGA ground motion relations for the geometric mean horizontal component of peak and spectral ground motion parameters, *Earthquake Spectra* **24**, 173–216.
- Dalguer, L. A., H. Miyake, S. M. Day, and K. Irikura (2008). Surface-rupturing and buried dynamic rupture models calibrated with statistical observations of past earthquakes, *Bull. Seismol. Soc. Am.* **98**, 1147–1161.
- Das, S. (1982). Appropriate boundary conditions for modeling very long earthquakes and physical consequences, *Bull. Seismol. Soc. Am.* **72**, 1911–1926.
- Day, S. M. (1982). Three-dimensional simulation of spontaneous rupture: The effect of nonuniform prestress, *Bull. Seismol. Soc. Am.* **72**, 1881–1902.
- Day, S. M., and C. R. Bradley (2001). Memory efficient simulation of anelastic wave propagation, *Bull. Seismol. Soc. Am.* **91**, 520–531.
- Frankel, A. (1995). Simulating strong motions of large earthquakes using recordings of small earthquakes: The Loma Prieta mainshock as a test case, *Bull. Seismol. Soc. Am.* **85**, 1144–1160.
- Frankel, A. (2009). A constant stress-drop model for producing broadband synthetic seismograms: Comparison with the Next Generation Attenuation relations, *Bull. Seismol. Soc. Am.* **99**, 664–680.

- Graves, R. W. (1996). Simulating seismic wave propagation in 3D elastic media using staggered grid finite differences, *Bull. Seismol. Soc. Am.* **86**, 1091–1106.
- Graves, R. W. (2008). The seismic response of the San Bernardino basin region during the 2001 Big Bear Lake earthquake, *Bull. Seismol. Soc. Am.* **98**, 241–252.
- Graves, R. W., and A. Pitarka (2004). Broadband time history simulation using a hybrid approach, *Proc. 13th World Conf. Earthq. Eng.*, Vancouver, Canada, paper no. 1098.
- Graves, R. W., B. T. Agaard, and K. W. Hudnut (2010). The ShakeOut earthquake source and ground motion simulations, *Earthquake Spectra*, in press.
- Guatteri, M., P. Mai, and G. Beroza (2004). A pseudo-dynamic approximation to dynamic rupture models for strong ground motion prediction, *Bull. Seismol. Soc. Am.* **94**, 2051–2063.
- Hanks, T. C., and R. K. McGuire (1981). The character of high-frequency strong ground motion, *Bull. Seismol. Soc. Am.* **71**, 2071–2095.
- Harris, R. A., and S. M. Day (1999). Dynamic 3D simulations of earthquakes on en echelon faults, *Geophys. Res. Lett.* **26**, 2089–2092.
- Hartzell, S. (1978). Earthquake aftershocks as Green's functions, *Geophys. Res. Lett.* **5**, 1–4.
- Hartzell, S., and T. H. Heaton (1983). Inversion of strong ground motion and teleseismic waveform data for the fault rupture history of the 1979 Imperial Valley, California, earthquake, *Bull. Seismol. Soc. Am.* **73**, 1553–1583.
- Hartzell, S., S. Harmsen, A. Frankel, and S. Larsen (1999). Calculation of broadband time histories of ground motion: Comparison of methods and validation using strong-ground motion from the 1994 Northridge earthquake, *Bull. Seismol. Soc. Am.* **89**, 1484–1504.
- Hartzell, S., P.-C. Liu, and C. Mendoza (1996). The 1994 Northridge, California, earthquake: Investigation of rupture velocity, rise time and high-frequency radiation, *J. Geophys. Res.* **101**, 20,091–20,108.
- Hartzell, S., G. Mariagiovanna, P. M. Mai, P.-C. Liu, and M. Fisk (2005). Calculation of broadband time histories of ground motion, Part II: Kinematic and dynamic modeling using theoretical Green's functions and comparison with the 1994 Northridge earthquake, *Bull. Seismol. Soc. Am.* **95**, 614–645.
- Hauksson, E., and J. Haase (1997). Three-dimensional V_p and V_p/V_s velocity models of the Los Angeles basin and central Transverse Ranges, California, *J. Geophys. Res.* **102**, 5423–5454.
- Herrero, A., and P. Bernard (1994). A kinematic self-similar rupture process for earthquakes, *Bull. Seismol. Soc. Am.* **84**, 1216–1228.
- Hillers, G., and S. G. Wesnousky (2008). Scaling relations of strike-slip earthquakes with different slip-rate dependent properties, *Bull. Seismol. Soc. Am.* **98**, 1085–1101.
- Hisada, Y. (2001). A theoretical omega-square model considering spatial variation in slip and rupture velocity, part 2: Case for a two-dimensional source model, *Bull. Seismol. Soc. Am.* **91**, 651–666.
- Hole, J. A., J. M. Stock, G. S. Fuis, M. J. Rymer, J. M. Murphy, R. R. Sickler, C. J. Criley, M. Goldman, R. D. Catchings, J. W. Ricketts, A. Gonzalez-Fernandez, N. Driscoll, G. Kent, A. J. Harding, and S. L. Klemperer (2009). The Salton Seismic Imaging Project (SSIP): Rift processes and earthquake hazards in the Salton Trough, *Eos Trans. AGU* **90**, no. 52, Fall Meet. Suppl. Abstract T31A-1790.
- Irikura, K. (1978). Semi-empirical estimation of strong ground motions during large earthquakes, *Bull. Disast. Prev. Res. Inst., Kyoto Univ.* **33**, 63–104.
- Joyner, W. B., and D. M. Boore (1986). On simulating large earthquakes by Green's function addition of smaller earthquakes, in *Earthquake Source Mechanics*, S. Das, J. Boatwright, and C. Scholz (Editors), American Geophysical Monograph 37, Maurice Ewing Vol. 6.
- Kagawa, T., K. Irikura, and P. Somerville (2004). Differences in ground motion and fault rupture process between surface and buried rupture earthquakes, *Earth Planets Space* **56**, 3–14.
- King, G. C. P., and S. G. Wesnousky (2007). Scaling of fault parameters for continental strike-slip earthquakes, *Bull. Seismol. Soc. Am.* **97**, 1833–1840.
- Liu, P., R. Archuleta, and S. H. Hartzell (2006). Prediction of broadband ground motion time histories: Frequency method with correlation random source parameters, *Bull. Seismol. Soc. Am.* **96**, 2118–2130.
- Mai, P. M., and G. C. Beroza (2002). A spatial random field model to characterize complexity in earthquake slip, *J. Geophys. Res.* **107**, no. B11, 2308, doi [10.1029/2001JB000588](https://doi.org/10.1029/2001JB000588).
- Marone, C., and C. H. Scholz (1988). The depth of seismic faulting and the upper transition from stable to unstable slip regimes, *Geophys. Res. Lett.* **15**, 621–624.
- Mikumo, Y. (1992). Dynamic fault rupture and stress recovery process in continental crust under depth-dependent shear strength and frictional parameters, *Tectonophysics* **211**, 201–222.
- Nielsen, S. B., and K. B. Olsen (2000). Constraints on stress and friction from dynamic rupture models of the 1994 Northridge, California, earthquake, *Pure Appl. Geophys.* **157**, 2029–2046.
- Olson, A. H., and R. J. Apsel (1982). Finite faults and inverse theory with applications to the 1979 Imperial Valley earthquake, *Bull. Seismol. Soc. Am.* **72**, 1969–2001.
- Ou, G.-B., and R. B. Herrmann (1990). A statistical model for ground motion produced by earthquakes at local and regional distances, *Bull. Seismol. Soc. Am.* **80**, 1397–1417.
- Pitarka, A., L. A. Dalguer, S. M. Day, P. G. Somerville, and K. Dan (2009). Numerical study of ground-motion differences between buried-rupturing and surface-rupturing earthquakes, *Bull. Seismol. Soc. Am.* **99**, 1521–1537.
- Pulido, N., and L. A. Dalguer (2009). Estimation of the high-frequency radiation of the 2000 Tottori (Japan) earthquake based on a dynamic model of fault rupture: Application to the strong ground motion simulation, *Bull. Seismol. Soc. Am.* **99**, 2305–2322.
- Saragoni, G. R., and G. C. Hart (1974). Simulation of artificial earthquakes, *Earthquake Eng. Structural Dyn.* **2**, 249–267.
- Schmedes, J., R. J. Archuleta, and D. Lavalle (2010). Correlation of earthquake source parameters inferred from dynamic rupture simulations, *J. Geophys. Res.* **115**, doi [10.1029/2009JB006689](https://doi.org/10.1029/2009JB006689).
- Schneider, J., W. Silva, and C. Stark (1993). Ground motion model for the 1989 M 6.9 Loma Prieta earthquake including effects of source, path, and site, *Earthquake Spectra* **9**, 251–287.
- Scholz, C. (2002). *The Mechanics of Earthquakes and Faulting*, Cambridge University Press.
- Shaw, B. E., and S. G. Wesnousky (2008). Slip-length scaling in large earthquakes: the role of deep penetrating slip below the seismogenic layer, *Bull. Seismol. Soc. Am.* **98**, 1633–1641.
- Shearer, P. M., G. A. Prieto, and E. Hauksson (2006). Comprehensive analysis of earthquake source spectra in southern California, *J. Geophys. Res.* **111**, B06303, doi [10.1029/2005JB003979](https://doi.org/10.1029/2005JB003979).
- Somerville, P. (1998). Utilization of strong motion data, in *Proc. of California Strong Motion Instrumentation Program*, M. Huang (Editor), Oakland, California, 15 September 1998.
- Somerville, P., and J. Yoshimura (1990). The influence of critical Moho reflections on strong ground motions recorded in San Francisco and Oakland during the 1989 Loma Prieta earthquake, *Geophys. Res. Lett.* **17**, 1203–1306.
- Somerville, P., K. Irikura, R. Graves, S. Sawada, D. J. Wald, N. Abrahamson, Y. Iwasaki, T. Kagawa, N. Smith, and A. Kowada (1999). Characterizing crustal earthquake slip models for the prediction of strong ground motion, *Seismol. Res. Lett.* **70**, no. 1, 59–80.
- Song, S. G., A. Pitarka, and P. Somerville (2009). Exploring spatial coherence between earthquake source parameters, *Bull. Seismol. Soc. Am.* **99**, 2564–2571.
- Tinti, Elisa, Eiichi Fukuyama, Alessio Piatanesi, and Massimo Cocco (2005). A kinematic source-time function compatible with earthquake dynamics, *Bull. Seismol. Soc. Am.* **95**, 1211–1223.
- Wald, D. J., and T. H. Heaton (1994). Spatial and temporal distribution of slip for the 1992 Landers, California, earthquake, *Bull. Seismol. Soc. Am.* **84**, 668–691.

- Wald, D. J., T. H. Heaton, and D. V. Helmberger (1991). Rupture model of the 1989 Loma Prieta earthquake from the inversion of strong motion and broadband teleseismic data, *Bull. Seismol. Soc. Am.* **81**, 1540–1572.
- Wald, D. J., T. H. Heaton, and K. W. Hudnut (1996). The slip history of the 1994 Northridge, California, earthquake determined from strong-motion, teleseismic, GPS, and leveling data, *Bull. Seismol. Soc. Am.* **86**, S49–S70.
- Wald, D. J., V. Quitoriano, T. H. Heaton, H. Kanamori, C. W. Scrivner, and C. B. Worden (1999). TriNet “ShakeMaps”: Rapid generation of peak ground motion and intensity maps for earthquakes in Southern California, *Earthquake Spectra* **15**, 537–556.
- Wald, D. J., B. C. Worden, V. Quitoriano, and K. L. Pankow (2005). ShakeMap manual: Technical manual, user’s guide, and software guide, *U.S. Geological Survey, Techniques and Methods 12-A1*, 132 pp.
- Walling, M., W. Silva, and N. Abrahamson (2008). Non-linear site amplification factors for constraining the NGA models, *Earthquake Spectra* **24**, 243–256.
- Wessel, P., and W. H. F. Smith (1998). New, improved version of the generic mapping tools released, *Eos Transactions AGU* **79**, 579.
- Wills, C., M. Petersen, W. Bryant, M. Reichle, G. Saucedo, S. Tan, G. Taylor, and J. Treiman (2000). A site conditions map for California based on geology and shear wave velocity, *Bull. Seismol. Soc. Am.* **90**, S187–S208.
- Zeng, Y., J. G. Anderson, and G. Yu (1994). A composite source model for computing realistic synthetic strong ground motions, *Geophys. Res. Lett.* **21**, 725–728.

Appendix

There are an infinite number of possible 2D wavenumber functions that satisfy the amplitude spectrum given by equation (1). However, not all of them represent physically realizable earthquake slip distributions. In particular, we limit our consideration to those functions that yield only positive values of slip and that also meet a prescribed mean slip value. A simple and effective way to do this is to generate the function by combination of a low-wavenumber deterministic part and a high-wavenumber stochastic part. This can be written as

$$U(k_s, k_d) = D(k_s, k_d)F + S(k_s, k_d)[1 - F], \quad (\text{A1})$$

where $U(k_s, k_d)$ is the 2D wavenumber representation of our desired slip function, $D(k_s, k_d)$ is the 2D Fourier transform of a prespecified deterministic slip function, $S(k_s, k_d)$ is the stochastic portion of the function (described in the following

text), and F is a wavenumber filter given by

$$F = [1 + (c_s^2 k_s^2 + c_d^2 k_d^2)^N]^{-1}, \quad (\text{A2})$$

with the wavenumber corners c_s^{-1} and c_d^{-1} specifying the transition between the deterministic and stochastic parts of the spectrum and N governing the sharpness of the transition.

The deterministic spectrum $D(k_s, k_d)$ is obtained by 2D Fourier transform of a tapered uniform slip distribution, such as that shown in Figure 1a. The filter parameters are $N = 1$, $c_s = L/2$, and $c_d = W/2$, where L and W are the fault length and width, respectively. This allows only the lowest wavenumbers from $D(k_s, k_d)$ to contribute to $U(k_s, k_d)$. For past earthquakes, $D(k_s, k_d)$ can be obtained from the 2D transform of a low-frequency slip distribution derived by waveform inversion, such as that shown in Figure 1c. In this case of the events studied here, we set $N = 4$, $c_s = dL$, and $c_d = dW$, where dL and dW are the subfault length and width of from the original slip-inversion model, respectively.

The stochastic portion of the function is given by

$$S(k_s, k_d) = \frac{D_0}{\sqrt{a_s a_d}} A(k_s, k_d) e^{i\theta}, \quad (\text{A3})$$

where $D_0 = D(0, 0)$, $A(k_s, k_d)$ is given by equation (1) and θ is a random number uniformly distributed between $-\pi$ and π . The factor $D_0/\sqrt{a_s a_d}$ ensures that the stochastic portion of the amplitude spectrum is properly scaled to the desired mean slip value.

URS Corporation
566 El Dorado St.
Pasadena, California 91101
robert_graves@urscorp.com
(R.W.G.)

BAE Systems
3060 Venture Lane, Suite 102
Melbourne, Florida 32934
(A.P.)